A time- and matrix-dependent TGFBR3–JUND–KRT5 regulatory circuit in single breast epithelial cells and basal-like premalignancies

Chun-Chao Wang[1], **Sameer S. Bajikar**[1], **Leen Jamal**[1,3], **Kristen A. Atkins**[2], and **Kevin A. Janes**[1,4]

[1]Department of Biomedical Engineering, University of Virginia, Charlottesville, Virginia 22908, USA

[2]Department of Pathology, University of Virginia, Charlottesville, Virginia 22908, USA

Abstract

Basal-like breast carcinoma is characterized by poor prognosis and high intratumor heterogeneity. In an immortalized basal-like breast epithelial cell line, we identified two anti-correlated gene-expression programs that arise among single extracellular matrix (ECM)-attached cells during organotypic 3D culture. The first contains multiple TGFβ-related genes including *TGFBR3*, whereas the second contains *JUND* and the basal-like marker, *KRT5*. TGFBR3 and JUND interconnect through four negative-feedback loops to form a circuit that exhibits spontaneous damped oscillations in 3D culture. The TGFBR3–JUND circuit appears conserved in some premalignant lesions that heterogeneously express KRT5. The circuit depends on ECM engagement, as detachment causes a rewiring that is triggered by RPS6 dephosphorylation and maintained by juxtacrine tenascin C, which is critical for intraductal colonization of basal-like breast cancer cells *in vivo*. Intratumor heterogeneity need not stem from partial differentiation and could instead reflect dynamic toggling of cells between expression states that are not cell autonomous.

INTRODUCTION

Genetically identical cells often coexist in different molecular states[1, 2]. Stochastic heterogeneities can drive cell fates in specific developmental contexts[3, 4]. Within mature

[4]Correspondence should be addressed to K.A.J. (kjanes@virginia.edu).
[3]Present address: Bioinformatics and Systems Biology Graduate Program, University of California at San Diego, San Diego, California 92093, USA

tissues, however, cell-autonomous heterogeneity is suppressed unless the molecular circuitry has been perturbed[5]. Cell-to-cell heterogeneity has been described in solid tumors, and heterogeneity within carcinoma cell lines has been associated with drug resistance[6–8].

Heterogeneity cannot be entirely explained by random biological noise—there are substantial contributions from a cell's local environment and its history[9, 10]. For most epithelial tissues, tracking cell-to-cell variability in time and space is difficult[11]. Organotypic 3D cultures allow monitoring of heterogeneity by supporting cells in reconstituted basement membrane[12–14]. The more realistic geometry and ECM context can give rise to non-genetic variations in molecular state[15, 16]. For instance, ECM-adhesion receptors comprise most of the stem-progenitor markers for heterogeneity in breast tissue and breast cancer[17, 18]. Organotypic heterogeneities might provide insight into clinical mechanisms of tissue-tumor heterogeneity that would otherwise be inaccessible.

Using 3D basement-membrane cultures of basal-like breast epithelia[12, 19], we have uncovered a dynamic heterogeneity that develops among ECM-attached cells during acinar formation. The expression circuit is composed of two anti-correlated transcriptional programs that establish a pair of expression states defined by *TGFBR3* and *JUND*. When this circuit is spontaneously excited, ECM-attached cells oscillate transiently and asynchronously between states, creating the static appearance of a cellular mosaic. Single-cell TGFBR3–JUND regulation tracks with heterogeneity of a cytokeratin (KRT5) diagnostic for ductal carcinomas *in situ* with basal-like features (basal-like DCIS). KRT5 correlations reverse upon detachment *in vitro* and in ECM-poor regions of basal-like DCIS, although availability of such samples was limited. We link the reversal to a keratinization process that is initiated by RPS6 dephosphorylation and maintained by expression of tenascin C (TNC). Disruption of TNC inhibits intraductal outgrowth of basal-like breast cancer cells *in vivo*, suggesting a functional role for the circuit during premalignancy. The dynamic and ECM-dependent transition of individual tumor cells between expression states may relate to the poor prognosis of heterogeneous basal-like breast cancer[20, 21].

RESULTS

Two co-existing single-cell states defined by *TGFBR3* and *JUND*

We recently described a random-sampling approach that profiles statistical fluctuations to uncover cell-to-cell heterogeneities in gene-expression regulation[16, 22]. Applying this "stochastic profiling" technique to a basal-like MCF10A cell clone cultured in basement membrane (Supplementary Fig. 1) identified 547 transcripts subject to strong heterogeneous regulation. 17% of transcripts fell into two clusters that were anticorrelated on a sampling-to-sampling basis (Fig. 1a,b). The first cluster included *TGFβ receptor III* (*TGFBR3*, a high-affinity TGFβ receptor[23]), *growth differentiation factor 11* (*GDF11*, a TGFβ-family ligand[24]), and *TGFβ-induced protein* (*TGFBI*, an ECM protein downstream of TGFβ-family signaling[25]). The co-occurrence of a TGFβ receptor, ligand, and marker protein suggested that the first cluster might be linked to TGFBR3-dependent signaling and gene expression.

The three TGFβ-related genes were strongly anticorrelated with the *jun D proto-oncogene* (*JUND*) (Fig. 1a,b), the only transcription factor in the second cluster, which comprised

mostly of protein biosynthetic genes[16]. We verified the single-cell anticorrelation by RNA FISH and showed that *JUND* and *TGFBR3* were expressed at reciprocal frequencies in ECM-attached cells (Fig. 1c–e). *TGFBR3* and *JUND* thus mark two states that basal-like cells spontaneously occupy when in contact with ECM.

TGFBR3–JUND heterogeneity is critical for normal acinar morphogenesis

TGFBR3 expression is strongly induced during organotypic culture (Fig. 2a)[26]. If *TGFBR3* upregulation occurred sporadically, it could explain the heterogeneous expression pattern observed among single ECM-attached cells (Fig. 1d). To test whether *TGFBR3* induction was important for acinar morphogenesis, we depleted TGFBR3 and verified specificity with an RNAi-resistant murine Tgfbr3 that is doxycycline (DOX) inducible (Tgfbr3 addback; Fig. 2b). Inhibiting *TGFBR3* upregulation caused a profound ductal-branching phenotype in ~30% of shTGFBR3 acini (Fig. 2c,d). Branching returned to baseline when Tgfbr3 was induced at day 4, the time when endogenous *TGFBR3* levels normally begin to rise (Fig. 2a,c,d). Thus, *TGFBR3* upregulation specifically suppresses ductal branching, conceivably by sensitizing cells to TGFβ-family ligands[23].

Unlike *TGFBR3, JUND* is easily detected under normal growth conditions and is frequently expressed in ECM-attached cells (Fig. 1e). To examine the role of sporadic *JUND* downregulation (Fig. 1d), we constitutively expressed HA-tagged JUND. This perturbation gave rise to stable cellular "bridges" across the acinar lumen, which are cytologically similar to the cribiform subtype of DCIS[27] (Fig. 2e–g). Heterogeneous *JUND* downregulation remained critical until late in morphogenesis, because induction of HA-JunD at day 9 caused cribiform acini weeks later (Supplementary Fig. 2a,b). To exclude artifacts caused by mild JUND overexpression, we coexpressed a stable shRNA against JUND together with an RNAi-resistant murine JunD that restored near-endogenous levels (Fig. 2h). This homogenization of *JUND* expression also caused cribiform acini (Fig. 2i). Therefore, heterogeneous regulation of *JUND* is critically important for acinar morphogenesis of basal-like cells.

TGFBR3–JUND signaling is oscillatory and dynamically coupled

To determine whether the TGFBR3–JUND clusters were functionally linked, we constitutively expressed TGFBR3 or JUND and analyzed endogenous mRNA levels of the other cluster (Fig. 3a–c). Constitutive JUND expression downregulated both *TGFBR3* ($P = 0.0026$, one-sided t test; Fig. 3a) and *TGFBI* ($P = 0.0027$, one-sided t test; Fig. 3b), suggesting that JUND antagonizes expression of the *TGFBR3* cluster. Ectopic *TGFBR3* expression reciprocally inhibited *JUND* expression ($P = 0.022$, one-sided t test; Fig. 3c), indicating that *JUND* does not simply act as an upstream repressor of the *TGFBR3* cluster. Mutual TGFBR3–JUND antagonism creates a double-negative (positive) feedback loop, which can establish two distinct molecular states[28].

Two other negative autoregulatory feedbacks were part of the overall wiring. Consistent with earlier reports[29, 30], constitutive JUND expression caused downregulation of endogenous *JUND* ($P = 0.043$, one-sided t test; Fig. 3c), and *TGFBR3* expression was acutely downregulated by TGFβ-family ligands ($P = 1.4 \times 10^{-5}$, one-sided t test; Fig. 3d).

These findings delineate a hybrid signaling-transcriptional circuit comprised of one positive-feedback and two negative-feedback loops (Fig. 3e).

Regulatory circuits with interlinked positive and negative feedback can oscillate between molecular states[28, 31]. We developed a live-cell imaging procedure for monitoring *TGFBR3* and *JUND* activities simultaneously. Active TGFβ-family signaling (TGFBR3*) was tracked by RFP1-labeled Smad2 (Fig. 3e and Supplementary Fig. 3a,b). For *JUND*, we engineered a rapidly responsive fluorescent reporter of endogenous promoter activity (Fig. 3e). We inserted ~2 kb of the *JUND* promoter (P_{JUND}) upstream of the fast-maturing YFP variant, Venus[32], which was destabilized by N-end rule fusion to ubiquitin C and C-terminal fusion to a PEST sequence[33, 34] (Supplementary Fig. 3c-e). Coexpression of ultradestabilized Venus (udsVenus) (P_{JUND}) and RFP1-Smad2 did not substantially perturb acinar morphogenesis relative to control cultures (Supplementary Fig. 3f-h), suggesting that endogenous TGFBR3–JUND pathways were not dramatically affected (Supplementary Fig. 3i-l). For 3D-culture experiments in which stable time-lapse imaging was successful, we repeatedly observed at-least one ECM-attached cell with coupled dual-reporter dynamics (Supplementary Video 1).

To compile two-color reporter activities across multiple experiments, we combined spectral filtering with algorithms from multiple-sequence alignment (see Methods). The aggregate alignment revealed that both reporters exhibited transient peaks of activity separated by 5–10 hr (Fig. 3f,g). When an ECM-attached cell remained in the optical plane long enough to observe two peaks, the second peak usually had smaller amplitude than the first, suggesting pathway damping (Fig. 3f, upper rows; Fig. 3g, middle rows). When the two reporters were compared within the same cell, dynamics were antiphase at nearly all time points[35]. Asynchronous, antiphase dynamics within the TGFBR3–JUND circuit provide a mechanism for the static anticorrelation observed in fixed specimens (Fig. 1).

We next used computational modeling to test whether the empirical circuit wiring could exhibit damped, antiphase responses like those observed in live cells (Fig. 3e, Supplementary Note 1, and Supplementary Data File 1). The circuit was modeled as a system of ordinary differential equations containing JUND (mRNA and protein) and TGFBR3 (mRNA, protein, and ligand-bound protein – TGFBR3*). We assigned basal synthesis and degradation rates to mRNA and protein species, and used Hill functions to capture transcription and feedback (see Methods and Supplementary Note 1). The live-cell reporters were encoded according to their mechanism of action and taken as outputs for the model.

We allowed the system to relax to steady state and then excited it with a modest 50% impulse of TGFBR3 activation, *TGFBR3* transcription, or *JUND* transcription. TGFBR3 activation yielded the clearest damped, antiphase oscillations (Fig. 3h), suggesting that the circuit could be endogenously triggered by TGFβ-family ligands, such as GDF11 (Fig. 1b) and others, which reside and accumulate in the ECM[36, 37]. We conclude that the specific feedback configuration is sufficient to cause the observed circuit dynamics (Fig. 3e-g).

The TGFBR3–JUND circuit is active in heterogeneous basal-like lesions

Cell-to-cell mosaicism is observed clinically in basal-like breast cancer, where ~50% of cases are highly heterogeneous for subtype-diagnostic cytokeratins[20, 38]. One such cytokeratin, *KRT5*, lies within the *JUND* cluster and is tightly coexpressed with *JUND* in ECM-attached cells[16]. The JUND–TGFBR3 expression circuit might therefore be engaged in basal-like carcinomas or premalignant lesions with basal-like features[39].

Using the transcriptional programs associated with *TGFBR3* and *JUND* (Fig. 1a), we examined transcript levels from a profiling study of 129 breast tumors from different subtypes[40]. Clustering separated the *TGFBR3–JUND* gene set into three groups (Fig. 4a). The first group was enriched for *JUND*-associated genes ($P = 6.6 \times 10^{-5}$, hypergeometric test), including *KRT5*, and was most-highly expressed in ER−–HER2− breast cancer, which contains the basal-like subtype[38]. The second group was enriched in *TGFBR3*-associated genes ($P = 2.1 \times 10^{-4}$, hypergeometric test) with mixed expression across different subtypes. The third group showed no significant enrichment ($P = 0.46$), yet was strongly downregulated in ER−–HER2− cases and contained both *JUND* and *TGFBR3*. We concluded that bulk-averaged measurements would be inadequate for characterizing JUND–TGFBR3 regulation in basal-like neoplasms[20].

To address this challenge, we collected an independent cohort of premalignant basal-like DCIS lesions with heterogeneous KRT5 expression[20, 39]. KRT5 indicates poor prognosis for basal-like carcinoma[21], and heterogeneous premalignancies would allow the cell-by-cell correlations of KRT5 to be examined with JUND and TGFBR3 while the tissue architecture was still intact. We therefore focused on the 8% of hormone-negative specimens diagnosed as DCIS to avoid complications associated with invasion and metastasis. We identified 22 archival cases that met these criteria along with four normal tissues obtained by reduction mammoplasty (Supplementary Table 1). In normal breast tissue, KRT5 and TGFBR3 were strongly expressed in the basal layer. KRT5 was predominantly localized to the ductal myoepithelia, whereas TGFBR3 was expressed mostly in the lobular myoepithelia (Fig. 4b). Conversely, JUND protein was very low in normal tissue but increased substantially in basal-like DCIS, where TGFBR3 was often undetectable (Fig. 4b). These results indicated a switch in TGFBR3–JUND–KRT5 regulation during premalignancy.

Next, we examined the coexpression of KRT5 and TGFBR3 or JUND in single cells by multicolor immunofluorescence. In the 59% of premalignant lesions where TGFBR3 could be detected, TGFBR3 and KRT5 expression remained mutually exclusive[41] (Fig. 4c and Supplementary Fig. 4a–c). This single-cell anticorrelation was consistent with both our retrospective analysis of invasive carcinomas and stochastic profiling of basal-like cultures (Fig. 1a and 4a). Conversely, cases with KRT5-positive regions of primary DCIS (41% of total) displayed a strong positive correlation between KRT5 and JUND among single cells (Fig. 4d and Supplementary Fig. 4d–f). Although the rarity of clinical samples limits the power of the present analysis, the agreement between the clinical and *in vitro* data suggests that basal-like ECM cultures might mimic the burst of proliferation and environmental stress experienced by early neoplasms[15, 19, 42].

JUND–KRT5 coexpression is modulated by ECM context

High-grade intraductal carcinomas frequently consist of a primary DCIS region along with secondary regions of "clinging carcinoma" (CC)[43]. CC forms when neoplastic cells disseminate intraluminally from the DCIS and cancerize peripheral breast lobules and ducts (Fig. 4e,f). Examination of CC regions showed anticorrelation of JUND and KRT5 (Fig. 4g and Supplementary Fig. 4g–i). JUND–KRT5 switching occurred without gross cytological changes in cases with both DCIS and CC (Fig. 4e,f,h–k). Tumor geography thus appeared to provide a form of external control on the TGFBR3–JUND expression circuit and its coregulation with KRT5.

The reversal of JUND–KRT5 coexpression prompted us to reexamine their relationship *in vitro*. During 3D culture, JUND and KRT5 proteins were coordinately expressed among outer cells (Fig. 5a). However, the JUND–KRT5 coexpression pattern was anticorrelated in interior cells. This transition could not have been anticipated by our initial profiling study, which focused exclusively on outer cells[16]. Nonetheless, the finding provided an independent replication of the JUND–KRT5 switching observed in basal-like tumors (Fig. 4d,g). This observation was corroborated in a few exceptional cases of DCIS where cells had detached partly or entirely from the tumor margin and JUND–KRT5 coexpression was reversed (Supplementary Fig. 4j–l).

To identify the molecular basis for the JUND–KRT5 inversion, we considered the variegated microenvironments of ECM cultures and human tumors. The most-recognized difference within ECM cultures is the spatially segregated access to basement membrane[19, 26, 44]. Outer cells contact the ECM-rich culture support and also secrete their own ECM molecules basolaterally[19, 45]. Inner cells are deprived of both these ECM sources and thus should be starved for integrin engagement. Analogously, in regions of DCIS, the local tumor stroma is potently activated, providing ECM to the primary tumor[46]. Cells in CC regions have left the primary site to colonize luminal, ECM-poor regions of the ductal tree and may behave like inner cells of the culture.

To simulate ECM deprivation, we placed cells in suspension culture. Before anoikis was evident, we observed clear and highly stereotyped changes in single-cell JUND–KRT5 expression. For the first 8 hr, JUND–KRT5 were coexpressed as double-positive or double-negative cells (Fig. 5b,c). At 24 hr, the $JUND^+$–$KRT5^+$ and $JUND^-$–$KRT5^-$ subpopulations became more clearly separated, when KRT5 increased with a filamentous pattern ($KRT5^F$) and anticorrelations started to appear. By 48 hr, $JUND^+$–$KRT5^F$ cells had vanished, and a fourth "keratinized" state emerged with intense KRT5 staining and no JUND protein or nuclear DNA ($KRT5^K$; Fig. 5b,c). Live-cell imaging showed that progression to the $JUND^-$–$KRT5^K$ state was rapidly executed, with keratinized skeletons eventually collapsing as cellular dust (Fig. 5c,d and Supplementary Fig. 5a). These late cellular steps are reminiscent of cornification, a cell-death process typically associated with skin[47].

Flow cytometry determined the high KRT5 ($KRT5^+$–$DAPI^+$) and $KRT5^K$ ($KRT5^+$–$DAPI^-$) cells to be minority populations (Fig. 5e,f and Supplementary Fig. 5b). Overall KRT5 levels increased during suspension culture, agreeing with the very high expression of single $KRT5^+$ cells (Fig. 5g and Supplementary Fig. 5b). KRT5 levels increased with two type I

keratin partners (KRT14 and KRT15; Supplementary Fig. 5c), supporting the execution of a specific keratin program in JUND$^+$–KRT5^F cells[48]. Vimentin remained mostly constant, but E-cadherin increased during keratinization and preceded the onset of anoikis by at least 24 hr (Supplementary Fig. 5c).

Endogenous JUND levels increased transiently before KRT5 upregulation (Fig. 5g), suggesting a role in the sequelae of ECM detachment. Although ectopic expression of JunD left the induction of KRT5 protein unaltered (Supplementary Fig. 5d), JunD-overexpressing cells largely remained in a double-positive state without overt keratinization ($P = 7.0 \times 10^{-5}$ and 3.0×10^{-6}, two-sided t test; Fig. 5h,i). Conversely, JUND knockdown accelerated keratinization and augmented it, with KRT5^K cells apparent as early as 8 hr (P = 2.4×10^{-4} and 8.7×10^{-4}, two-sided t test; Fig. 5j,k), even though KRT5 upregulation was unaffected (Supplementary Fig. 5e). We conclude that JUND restrains detachment-induced keratinization but is independent of the upregulation of KRT5 itself.

Detachment-induced KRT5 upregulation is triggered posttranscriptionally by loss of phosphorylated RPS6

To identify the mechanism of detachment-induced KRT5 upregulation, we used 3D ECM cultures and small-sample cDNA amplification[16, 22] to profile mRNA expression globally within developing acini (Fig. 6a). Matrix-attached and matrix-deprived cells were isolated by laser-capture microdissection at day 6, when inner versus outer cell fates have just stabilized but later programs have not yet been fully engaged[15, 42]. Transcriptional profiling of each subpopulation revealed divergent regulation of *JUND* and *KRT5* mRNA. *KRT5* levels were proportionally lower (and *JUND* levels higher) in inner ECM-deprived cells, contrasting the changes in KRT5–JUND protein observed in suspension (Fig. 5g, 6b). To exclude that the discrepancies were due to differences in assay format, we quantified *KRT5* and *JUND* transcripts in suspension and observed similar mRNA changes as in microdissected cells ($P = 0.014$ and 1.5×10^{-4}, two-sided t test; Fig. 6c,d). This indicated that KRT5 protein upregulation did not result from increased gene expression.

Surveying the entire cluster for matrix-dependent transcripts that correlated with *KRT5* or *JUND*, we identified the ribosomal protein *RPS6,* which showed proportionally decreased expression in ECM-deprived inner cells (Fig. 6e). Unlike *KRT5, RPS6* was not downregulated in suspension cells (Fig. 6f). We attribute this difference to the *RPS6* increase that occurs with time in 3D culture, presumably in matrix-attached cells (Fig. 6g). Notwithstanding, we found that RPS6 was required for detachment-induced upregulation of KRT5, with keratinization observed only in cells that had escaped knockdown (Supplementary Fig. 6a-d). This implicated a translational mechanism that depended specifically on the status of RPS6.

RPS6 is the canonical substrate of S6 kinase (S6K), which is activated by integrin engagement and inactivated by detachment[49, 50]. When 3D cultures were stained for RPS6 phosphorylation (p-RPS6), we observed no immunoreactivity among inner cells (Fig. 6h). In suspension culture, loss of p-RPS6 occurred acutely after 8 hr (Fig. 6i). To reconstitute p-RPS6, we inducibly overexpressed a constitutively active S6K (E389- CT) mutant [51] (Supplementary Fig. 6e,f). DOX treatment at 8 hr after detachment maintained a suprabasal

level of p-RPS6 in a fraction of the population and attenuated keratinization at 24 hr (P = 0.014, two-sided t test; Fig. 6j-l and Supplementary Fig. 6g). To test if RPS6 dephosphorylation was sufficient to induce keratinization, we treated adherent cells with inhibitors of TORC1 or S6K (Supplementary Fig. 6h). All inhibitors reduced RPS6 phosphorylation and caused sporadic keratinization in attached cells, whereas MEK1/2 inhibition did not (Supplementary Fig. 6i). Thus, loss of p-RPS6 is a critical trigger for detachment-induced keratinization of basal-like breast epithelial cells.

Stabilization of anticorrelated JUND–KRT5 by TNC

Keratinization provided an appealing mechanism for the JUND–KRT5 anticorrelation observed in inner cells and CC regions of basal-like breast cancer (Fig. 4g and 5a). However, it was unclear why JUND$^+$–KRT5$^-$ cells would exist if detachment from ECM rapidly caused irreversible loss of JUND and upregulation of KRT5. The JUND–KRT5 staining pattern revealed that keratinized JUND$^-$–KRT5^K cells were often surrounded by JUND$^+$–KRT5$^-$ cells (Fig. 5a), suggesting that JUND$^-$–KRT5^K cells could be exchanging juxtacrine signals with JUND$^+$–KRT5$^-$ cells.

To identify candidate ECM ligands that could fulfill this role, we screened breast cancer immunohistochemistry images from The Human Protein Atlas[52, 53]. Among 71 ligands[54], only the matricellular protein TNC[55] was expressed heterogeneously in a cell-intrinsic manner within CC regions of breast carcinoma (Supplementary Table 2 and Supplementary Fig. 7a,b). TNC is important in early colonization of breast-cancer metastases to the lung[56]. Sporadic TNC expression has also been noted in basal keratinocytes[57], suggesting a connection to epidermal keratinization. We hypothesized that TNC could stabilize JUND$^+$–KRT5$^-$ cells if it were endogenously expressed *in vitro* and *in vivo*.

In ECM cultures, we found inner cells that strongly expressed TNC (Fig. 7a). Interestingly, JUND$^+$–KRT5$^-$ cells appeared to extend lamellipodia around TNC$^+$–JUND$^-$–KRT5^K skeletons (Fig. 7a, inset), suggesting extensive adhesive contacts. In CC regions of basal-like premalignancies, TNC$^+$–JUND$^-$–KRT5$^+$ cells were similarly in direct apposition with cells that were JUND$^+$–KRT5$^-$ (Fig. 7b and Supplementary Fig. 7c–h). Following ECM withdrawal, TNC was strongly upregulated in the KRT5^F and KRT5^K subpopulations (Fig. 7c and Supplementary Fig. 7i–k). Unlike other keratinization-related programs, TNC upregulation may be transcriptionally mediated (Supplementary Fig. 7j). Only 2–6% of detached cells expressed TNC, but ~60% of keratinized cells were TNC$^+$ (Supplementary Fig. 7l-n). When TNC was added to 2D cultures of basal-like breast epithelia, the single-cell JUND–KRT5 correlation reversed (Fig. 7d), illustrating that TNC actively participates in anticorrelating JUND and KRT5 expression.

To determine whether TNC could explain the JUND–KRT5 mosaicism in ECM-poor microenvironments, we built a multi-cell agent-based model of CC[58] (Supplementary Note 1 and Supplementary Data File 2). We coded for an arbitrary CC geometry, where individual cancer cells ("agents") spontaneously keratinize as a function of their JUND–KRT5 levels and the neighboring expression of TNC (see Methods). Without TNC, virtually all cells keratinized (Fig. 7e), consistent with the irreversibility of keratinization in the model. By contrast, including TNC caused a stable mosaic of cells that were JUND$^-$–KRT5^K or

JUND$^+$–KRT5$^-$ (Fig. 7f). This model made two predictions that were subsequently verified in clinical specimens. First, keratinization should be extensive among cells immediately adjacent to the lumen because of fewer opportunities to be stabilized by adjacent TNC-positive cells (Fig. 7f, solid). Retrospectively, we identified many stretches of keratinized cells along CC lumina (Fig. 4g, 7g, and Supplementary Fig. 4g,i, S7c,g). Second, the model predicted multi-cellular clusters that were locally homogeneous for JUND (Fig. 7f, dashed), because JUND increases up until keratinization occurs (Fig. 5g) and TNC-positive cells "corral" the multi-cellular clusters at different times during the model simulation. A similar mechanism may operate in CC, because we observed several multi-cell clusters with roughly equal JUND expression, even though lesions were heterogeneous overall (Fig. 4g, 7g, and Supplementary Fig. 4g–i, S7c,g). We conclude that keratinization—triggered by detachment-induced RPS6 dephosphorylation and modulated by TNC—is responsible for the single-cell anticorrelation of JUND–KRT5 in basal-like CC.

TNC promotes intraductal colonization of detached basal-like breast cancer cells *in vivo*

We sought to examine the importance of keratinization for cancer cell survival in realistic ECM-poor environments. Following prolonged detachment, the basal-like breast cancer line MDA-MB-468 showed reduced RPS6 phosphorylation and JUND expression and upregulation of KRT5 (Fig. 8a). Pharmacologic inhibition of RPS6 also caused keratinization in attached MDA-MB-468 cells (Supplementary Fig. 8a), indicating that the JUND-KRT5 circuitry was largely preserved in this cancer line. Similar results were obtained with a variant of MCF10A cells expressing oncogenic Ras (MCF10DCIS.com[59]; Supplementary Fig. 8b,c), indicating that the circuit is not disrupted by cell transformation. When MDA-MB-468 cells were injected intraductally into SCID-beige mice[60], they resembled detached neoplastic cells in basal-like premalignancies (Fig. 8b,c).

To evaluate the importance of TNC in ECM-limited microenvironments *in vivo*, we transduced luciferase-expressing MDA-MB-468 cells with an inducible shTNC hairpin[56] (Fig. 8d) and monitored tumor-cell survival following intraductal injection. TNC knockdown significantly increased the percentage of KRT5$^+$ cells ($P = 0.0014$, two-sided t test; Fig. 7e, 8e). Two days after injection, we observed comparable bioluminescence in ducts injected with TNC knockdown cells compared to uninduced controls (Supplementary Fig. 8d). At 21 days, however, colonization frequency was significantly inhibited by TNC knockdown ($P = 0.049$, Fisher's exact test; Fig. 8f). When shTNC cells were cultured in suspension, the pattern of apoptotic cells was also significantly affected ($P = 0.0002$, two-way ANOVA; Supplementary Fig. 8e). Analysis of injected glands with detectable bioluminescence showed viable proliferating cells together with evidence of anoikis (Supplementary Fig. 8f). There was strong TNC immunoreactivity next to viable cells in control ducts, which was virtually eliminated in ducts injected with induced shTNC cells (Fig. 8g,h). Among the largest tumors, TNC expression exhibited a punctate pattern analogous to that observed in human breast cancers (Fig. 8i). Human TNC expression was also detected in the largest DOX-treated tumor, indicating that it had escaped TNC knockdown (Supplementary Fig. 8g). These xenograft experiments suggest that TNC provides a critical survival signal for neoplastic cells that would otherwise undergo keratinization or anoikis during premalignancy. Our results indicate that the TGFBR3–

JUND–KRT5 expression circuit exhibits its own internal dynamics but is also subject to external control by the local ECM *in vitro* and *in vivo*.

DISCUSSION

By profiling expression heterogeneities in a relevant ECM context, we have uncovered a major signaling circuit within basal-like breast epithelia. Cells in contact with basement membrane undergo transient oscillations between two molecular states defined by their *TGFBR3–JUND* expression. Perturbation of either state disrupts normal acinar morphogenesis. Proper dynamic regulation of the circuit is critical for establishing and stabilizing the identity of ECM-attached cells. By extension, proliferating neoplasias may reengage the TGFBR3–JUND circuit in search of a cell fate amidst a heterogeneous ECM microenvironment.

Our study began with a transcriptional dichotomy between two single-cell expression states, but the overall circuit extends beyond transcription. Circuit activation in ECM-attached cells likely occurs by posttranslational signaling from TGFβ-family receptors. Interestingly, TGFβ ligands bind ECM and exist as latent complexes that become disinhibited by mechanical force[61]. Considering that breast epithelia are known to be mechanoresponsive[62], the earliest trigger for circuit oscillations may be changes in local cell-ECM mechanics.

There also appears to be a critical posttranscriptional component regulated by phosphorylation of RPS6. Phosphorylated RPS6 often promotes selective translation of certain mRNA species, but p-RPS6 and translation can be uncoupled[63]. Surprisingly, KRT5 levels increase, rather than decrease, following loss of RPS6 phosphorylation. This could due to increased KRT5 translation or improved stability as a filament pair with a type I keratin. Other type II keratins are posttranscriptionally regulated[64], although the precise mechanisms remain elusive.

The ECM-dependent relationship between KRT5 and TGFBR3–JUND is reflected both in basal-like cultures and preinvasive basal-like neoplasias (Fig. 8j). Outer ECM-attached cells of cultured acini and primary DCIS show correlated expression of JUND–KRT5. By contrast, the inner ECM-deprived cells of a 3D acinus may mimic facets of preinvasive dissemination that partly explain the macroscopic heterogeneity of clinical specimens (Fig. 8l). Detached epithelial cells stochastically execute a keratinization program[48], which delays anoikis by creating a TNC mosaic within 3D cultures and in CC. Breast-cancer patients with TNC-positive tumor cells frequently have lymph-node metastases and very-poor prognosis[65]. Our data build on recent animal models[56] by suggesting that juxtacrine TNC may be critical for secondary orthotopic colonization within the duct.

The most-recognized driver of late-stage tumor heterogeneity is genomic instability, but how heterogeneous tumors evolve from premalignancy has been more enigmatic. Our work places renewed emphasis on the microenvironment and the dynamic asynchronicity of the constituent cells. Reversible lineage switching has been described in several contexts[66, 67], suggesting together with our results that breast cancer may be more dynamic than previously appreciated.

METHODS

Cell lines and 3D culture

The MCF10A-5E clone was previously reported and was grown in organotypic 3D culture as described for MCF10A cells[12, 16]. MCF10DCIS.com cells[59] were originally obtained from Wayne State University and cultured in DMEM/F-12 medium (Invitrogen) plus 5% horse serum (Invitrogen). MDA-MB-468 cells were obtained from ATCC and cultured in L-15 medium (Invitrogen) plus 10% fetal bovine serum (Hyclone) without supplemental CO_2.

Plasmids

pLKO.1 shGFP puro (Addgene #12273), pLKO.1 shTGFBR3 puro (TRCN0000033430), and pLKO.1 shJUND puro (TRCN0000014974) were obtained from The RNAi Consortium[68] or Addgene. pBabe JunD-HA neo, pBabe JUND-HA neo, pBabe RFP1-Smad2 neo, pBabe JunD-Venus puro, and pBabe RFP1-KRT5 hygro were constructed by PCR cloning from plasmid templates (Open Biosystems) into the retroviral vector pBabe neo, pBabe puro, or pBabe hygro. S6K (E389-ΔCT) was excised from pRK7-HA-S6K1-E389-ΔCT (Ref. [51]) by restriction digest with *XbaI* and *EcoRI*. Doxycycline-inducible Tgfbr3-HA, JunD-HA and S6K (E389-ΔCT) expression vectors were constructed by PCR cloning or subcloning into the entry vector pEN_TTmiRc2, followed by LR recombination into the lentiviral vector pSLIK neo[69]. The human TRIPZ lentiviral inducible shRPS6 constructs V3THS_333416 (#1) and V3THS_333414 (#2) and the shTNC construct V2THS_133229 (Ref. [56]) were obtained from Open Biosystems. pLenti PGK Blast V5-LUC (w528-1) was obtained from Addgene.

pTRF.1 udsVenus (P$_{JUND}$) was constructed starting with the commercial lentiviral vector, pTRF1-mCMV-dscGFP (System Biosciences). First, cGFP was excised from pTRF1-mCMV-dscGFP by restriction digest with *HindIII* and *EcoRV*, and the vector was ligated with a similarly digested Venus[32] prepared by PCR cloning designed to contain the appropriate motif for N-end rule degradation[32, 34]. The resulting pTRF.1-mCMV-dsVenus was then digested with *HindIII*, dephosphorylated, and ligated with a similarly digested ubiquitin C monomer prepared by PCR cloning from oligo(dT)-primed MCF10A-5E cDNA to produce pTRF.1-mCMV-udsVenus. Last, this vector was digested with *EcoRI* and *SpeI* and ligated with a similarly digested P$_{JUND}$ prepared by PCR from MCF10A-5E genomic DNA to produce pTRF.1 udsVenus (P$_{JUND}$). All constructs were verified by sequencing.

Viral transduction

Lentiviruses were prepared in 293T cells (ATCC) by triple transfection of the lentiviral vector together with psPAX2 + pMD.2G (Addgene) and transduced into MCF10A-5E, MDA-MB-468, and MCF10DCIS.com cells as described previously[42]. Retroviruses were similarly prepared by double transfection of the pBabe construct together with pCL ampho (Addgene) and transduced into MCF10A-5E cells as described previously[42]. For viral vectors carrying selectable markers, transduced cells were selected in growth medium containing 2 μg/ml puromycin, 300 μg/ml G418, 100 μg/ml hygromycin, or 4–6 μg/ml blasticidin until control plates had cleared. For addback experiments, viral titers were

adjusted to match the endogenous protein expression as closely as possible. For live-cell reporters, we used the minimum viral titer that gave sufficient signal above background for long-term imaging. For pTRF.1 udsVenus (P$_{JUND}$), which lacks a selectable marker, transduced cells were flow sorted for baseline Venus fluorescence at the University of Virginia Flow Cytometry Core Facility.

RNA FISH

Acinar cultures were embedded at day 10 of morphogenesis. Single- and multi-color RNA FISH on 5 μm cryosections was performed as described previously[16, 42].

Quantitative PCR

Quantitative PCR was performed as described elsewhere[70]. Primer sequences are as follows: *TGFBR3*, 5'- tgtcacctggcacattcatt -3' (forward), 5'- acaggatttgccatgcattt -3' (reverse); *TGFBI*, 5'- ctatgccaagtccctggaaa -3' (forward), 5'- cctccaagccacgtgtagat -3' (reverse); *JUND*, 5'- cgttggttgtgtgtgtgtgt -3' (forward), 5'- ggcgaaccaaggattacaaa -3' (reverse); *KRT5*, 5'- tttgtctccaccacctcctc -3' (forward), 5'-cctgggaaccaaagaatgtg -3' (reverse); *RPS6*, 5'- ccccaaaagagctagcagaa -3' (forward), 5'- ctgcaggacacgtggagtaa -3' (reverse); *TNC*, .5'- aaccccaggagtttgagacc –3' (forward), 5'- gggctccagtgattttccta -3' (reverse).

Immunoblotting

MCF10A-5E cells expressing the indicated constructs were lysed in 50 mM Tris (pH 8.0), 150 mM NaCl, 5 mM EDTA, 1% Triton X-100, 0.1% SDS, 0.5% sodium deoxycholate. 20–30 μg of clarified extract was separated on an 8 or 10% SDS-PAGE gel and transferred to PVDF (Immobilon-FL, Millipore). Membranes were blocked with 0.5× Odyssey blocking buffer (LI-COR, 1:1 in PBS) and incubated overnight at 4°C in 0.5× Odyssey blocking buffer (LI-COR) + 0.1% Tween, containing one of the following primary antibodies: TGF-β Receptor III (1:1000, Cell Signaling, #2519), HSP 90α/β (H-114) (1:1000, Santa Cruz, sc-7947), Jun D (329) (1:1000, Santa Cruz, sc-74), S6 Ribosomal Protein (54D2) (1:1000, Cell Signaling, #2317), Phospho-S6 Ribosomal Protein (Ser240/244) (D68F8) (1:1000, Cell Signaling, #5364), α/β-tubulin (1:1000, Cell Signaling, #2148), α-tubulin (1:20,000, Abcam, ab89984), β-actin (1:1000, Ambion, #AM4302), Keratin 5 (1:1000, Covance, SIG-3475), Keratin 14 (1:1000, Covance, PRB-155P), Smad2 (L16D3) (1:1000, Cell Signaling, #3103), GFP (1:1000, Invitrogen, A-11122), Tenascin (BC-24) (1:1000, Sigma, T2551), vimentin (SP20) (1:100, Abcam, ab16700), E-cadherin (36) (1:1000, BD Biosciences, #610182), caspase-3 (1:1000, Cell Signaling, #9662), and KRT15 (1:1000, Thermo, MA5-15567). Membranes were washed 4 × 5 minutes in PBS-T (PBS + 0.1% Tween) and incubated for 1 hr at room temperature in secondary antibody solution (0.5× Odyssey blocking buffer + 0.01% SDS + 0.1% Tween) containing IrDye 800 or IrDye 680LT-conjugated secondary antibody (1:20,000, LI-COR). Membranes were washed 4 × 5 minutes in PBS-T, rinsed with PBS, and imaged by infrared fluorescence on a LI-COR Odyssey instrument. Relative band intensities were quantified by densitometry with ImageJ.

Clinical samples

The pathology database at the University of Virginia from 2004–2012 was searched for all cases of high-grade DCIS, since this is the cohort that contains the basaloid subgroup. The set was then searched for estrogen receptor status and only those that were ER negative were selected. The search was confined to 2004 and later because 2004 was the year pathologists began reflexively testing DCIS for estrogen receptor status. All cases with an invasive carcinoma component were excluded. This resulted in 5–7 cases per year. The cases were deidentified for any patient demographics and used for immunohistochemical analysis of cytokeratin 5/6. Samples that were positive for cytokeratin 5/6 were followed up with a panel of six immunohistochemical markers: p53 (11/22 positive), E-cadherin (22/22 positive), KRT18 (21/22 positive), p63 (1/22 positive), smooth-muscle actin (21/22 positive), and vimentin (6/22 positive) (Supplementary Table 1). All clinical work was done according to a protocol under IRB-HSR approval #14176 and PRC approval #1363 (502-09).

Immunofluorescence

Immunofluorescence in frozen sections or on coverslips was performed as described previously[42] using the following primary antibodies: Cytokeratin 5/6 (D5/16 B4) (1:200, Dako, M7237), Keratin 5 (1:5000, Covance, SIG-3475), Tenascin (BC-24) (1:2000, Sigma, T2551), Jun D (329) (1:500, Santa Cruz, sc-74), or Phospho-S6 Ribosomal Protein (Ser240/244) (D68F8) (1:1000, Cell Signaling, #5364). For paraffin sections, slides underwent antigen retrieval before immunostaining as described for TGFBR3 below. Whole-mount immunofluorescence of day 10 acini was performed as described previously[42] using the following primary antibodies: E-cadherin (36) (1:500, BD Biosciences, #610182) or HA (3F10) (1:200, Roche, #11815016001).

Two-color time-lapse confocal imaging

Live-cell experiments involved MCF10A-5E cells stably transduced with pTRF.1 udsVenus (P_{JUND}) and pBabe RFP1-Smad2 neo as described above. For long-term live-cell imaging of 3D acini, a plastic coverslip was cut to size and placed at the base of an 8-well chamber slide (BD Biosciences) before starting. Coverslipped chamber slides were then coated with Matrigel (BD Biosciences), and cells were grown in organotypic 3D culture as described for MCF10A cells[12]. At day 10, the Matrigel-coated plastic coverslip containing adherent 3D acini was removed and flipped upside down into a culture dish with a fused glass coverslip (MatTek) filled with conditioned medium from the 3D culture. A second glass coverslip was placed on top of the inverted plastic coverslip, and the air-tight reservoir was sealed by applying high vacuum grease (Dow Corning) followed by a mixture of Vaseline, lanolin, and paraffin. The sealed reservoir was then covered with light mineral oil to prevent evaporation during imaging.

Live acinar cultures were maintained at 37°C with a heated blower. Time-lapse imaging was performed using a laser scanning confocal microscope (LSM 700, Carl Zeiss) equipped with an EC Plan-Neofluar 40x/1.30 oil-immersion objective and four diode lasers (5–10 mW) centered at 405, 488, 555, and 639 nm. udsVenus was excited at 488 nm and its emission detected between 488 and 585nm. RFP1 was excited at 555 nm and its emission detected

above 582 nm. The confocal pinhole was kept at 1 Airy unit, and laser powers were typically set at 2–5% to minimize photobleaching. Time-lapse images were acquired every 15 minutes for 15–20 hr. Image assembly and processing were performed using MetaMorph (Molecular Devices).

Image segmentation and quantification

Single cells and nuclei from live-cell images were manually segmented and applied to the RFP1 and udsVenus fluorescence stacks to calculate median nuclear, cytoplasmic, and total fluorescence intensities. The RFP1-Smad2 signal was evaluated as the ratio of median nuclear-to-cytoplasmic fluorescence. The median total udsVenus fluorescence per cell was normalized to the overall fluorescence intensity of cells in the same frame to account for photobleaching.

For RNA FISH scoring, single ECM-attached cells were manually binned into high expression and low-no expression based on DNP-labeled riboprobe staining intensity. A minimum of 150 cells was scored per hybridization across four independent hybridizations.

Time course alignment

Data from live cell imaging time courses were spectrally decomposed with the fft function in MATLAB, smoothed by low-pass filtering at $8.6e^{-5}$ Hz, and then reconstructed with the ifft function in MATLAB. After spectral filtering, individual time courses were standardized and clustered hierarchically based on the joint alignment of the RFP1-Smad2 and udsVenus traces between experiments. The alignment algorithm is based on a full sliding window of both traces with zero gaps and a cost function that uses the sum-of-squared difference between the two experiments to be aligned, scaled by the extent of overlap between them. All possible experiment pairs and alignments within the dataset were considered, and the experiments with the best pairwise alignment were combined by average linkage. The exhaustive pairwise comparisons and linkages were repeated until all of the independent experiments were aligned. In the final pairwise comparison, one of two nearly equivalent alignments was visually selected.

Computational modeling

The TGFBR3–JUND circuit was modeled as a system of coupled ordinary differential equations. mRNA and protein species were assigned basal synthesis and degradation rates as described in Supplementary Note 1. Transcriptional inhibition steps were modeled using the Hill equation without cooperativity, and feedback strengths were adjusted manually as free parameters to reproduce the damped periodicity observed experimentally. Sensitivity analysis on the manually adjusted parameters is described in Supplementary Note 1. The model was simulated with ode15s in MATLAB and allowed to reach steady state before exciting the system with a 50% increase in the appropriate reaction rate for 1 hr. Code for the simulations in Fig. 3h is available in the Supplementary Data File 1.

The agent-based model of CC was constructed using NetLogo v4.1.1 (http:// ccl.northwestern.edu/netlogo/). Single cells were seeded at a predefined geometry and initialized with the same basal level of KRT5 and JUND. During each time step of the

simulation, KRT5 and JUND were incremented by a uniform pseudorandom number between zero and one [U(0,1)] that was inversely scaled by the number of neighboring

TNC-positive cells (TNC$^+$) as follows: $\frac{U(0,1)}{2^{TNC^+}}$. Since JUND inhibits late keratinization (Fig. 5h,i), the fluctuating JUND–KRT5 difference was used as a proxy for keratinization. The JUND–KRT5 difference was evaluated after each time step, and keratinization occurred when the difference reached a critical negative threshold. Keratinized cells then expressed TNC and were no longer incremented for KRT5 or JUND expression. The model was run until steady state, and the final display was used as the model output. Simulations with alternative geometries are described in Supplementary Note 1, and code for the models in Fig. 7e,f is available in the Supplementary Data File 2.

Clustering analysis

All unsupervised hierarchical clustering analysis was performed in MATLAB (Mathworks) using the Bioinformatics toolbox with Euclidean distance and Ward's linkage. For the retrospective analysis of clinical samples, the microarray dataset[40] was mined for probesets matching the genes in the TGFBR3 and JUND clusters (Fig. 1a). Probesets were median centered and scaled to interquartile range before clustering, TGFBR3 and JUND enrichment within the final dendrogram was assessed by hypergeometric test.

Immunohistochemistry

4 μm paraffin tissue sections were processed according to the optimal conditions for the target antigen. For TGFBR3 and KRT5, antigen retrieval and deparaffinization were performed with a PT Link (Dako) using low-pH (KRT5) or high-pH (TGFBR3) EnVision FLEX Target Retrieval Solution (Dako) for 20 minutes at 97°C. For JUND, sections were dewaxed through a graded alcohol series and used without antigen retrieval. Endogenous peroxidases were blocked with peroxidase and Alkaline Phosphatase Blocking Reagent (Dako) according to the manufacturer's recommendations. Sections were then incubated with one of the following primary antibodies for 30 minutes at room temperature: TGFBR3 (1:100, Sigma, HPA008257), Cytokeratin 5/6 (D5/16 B4) (1:100, Dako, M7237), Keratin 5 (1:5000, Covance, SIG-3475), Tenascin (BC-24) (1:2000, Sigma, T2551), Jun D (329) (1:200, Santa Cruz, sc-74), estrogen receptor (1:100, Biocare Medical, ACA 301), p53 (1:200, Dako, M7001), E-cadherin (1:4000, Epitomics, 1702-1), KRT18 (1:100, Epitomics, 1433-1), p63 (1:2000, Sigma, P3737), smooth muscle actin (1:200, Epitomics, 1184-1), vimentin (1:200, Epitomics, 4211-1), Ki67 (1:400, Epitomics, 4203-1), and cleaved PARP (1:500, Epitomics, 1051-1). Primary antibodies were detected using Envision Dual Link (Dako) followed by incubation with 3,3'-diaminobenzidine tetrahydrochloride (DAB+) chromogen (Dako). Immunohistochemistry with murine antibodies on mouse tissue was performed with UltraVision Quanto mouse-on-mouse horseradish peroxidase (Fisher). Sections were counterstained with hematoxylin and then dehydrated, cleared, and mounted. Images were captures on a 3.3-million pixel QColor3 camera (QImaging), and image levels were equally scaled and auto toned in Photoshop.

Suspension assays

MCF10A-5E cells expressing the indicated constructs were trypsinized and plated at 400,000 cells/ml in assay medium containing 5 ng/ml EGF on poly-(2-hydroxyethyl methacrylate) (poly-HEMA) coated tissue culture plates. At the indicated time points, medium was removed by centrifugation at 150 rcf for 3 minutes. Cells were washed with 500 μl ice-cold PBS. For immunoblotting, cells were lysed in 62.5 mM Tris (pH 6.8), 2% SDS, 10% glycerol, 0.01% bromphenol blue, 2.5% EtOH (0.04%), 100 mM DTT, and whole-cell extracts were separated on 6% or 12% SDS-PAGE gel. For immunofluorescence, cells were fixed with 3.7% PFA at room temperature for 15 minutes, permeabilized with 0.3% Triton X-100 in PBS, and then processed for immunofluorescence as described above. For live-cell imaging, MCF10A-5E cells expressing JUND-Venus and RFP1-KRT5 were cultured on poly-HEMA-coated culture dishes with a fused glass coverslip (MatTek). Time-lapse imaging was performed as described above.

Flow cytometry

Cells were dissociated with Accutase (Invitrogen) for 1 hr at 37°C, fixed with 3.7% PFA, permeabilized with ice-cold methanol, and stored at -20°C. Cells were blocked with 1× Western blocking reagent (Roche) in PBS-T for 30 minutes and incubated 1 hr at room temperature with the following primary antibodies: Jun D (329) (1:100, Santa Cruz, sc-74), Keratin 5 (1:20,000, Covance, SIG-3475), Tenascin (BC-24) (1:200, Sigma, T2551), Cleaved Caspase-3 (Asp175) (1:200, Cell Signaling, #9661), Cleaved PARP (Asp 214) (1:200, BD Pharmingen, 552597), HA (3F10) (1:200, Roche, #11815016001). Cells were washed in PBS-T, incubated for 1 hr at room temperature with Alexa Fluor 488-, phycoerythrin-, and Alex Fluor 647-conjugated secondary antibodies (Invitrogen and Jackson ImmunoResearch), and counterstained with DAPI. Because collapsed cells are probably lost during this dissociation and staining procedure (Supplementary Figure 5a), the flow cytometry quantification of KRT5^K frequency is likely an underestimate.

Cells were analyzed on a BD FACSCalibur flow cytometer, equipped with 407-nm, 488-nm, 561-nm, and 637-nm lasers (BD Biosciences). For DAPI, data were collected with the 407-nm laser and 445/30 or 450/50 nm bandpass filter. For Alexa Fluor 488, data were collected with the 488-nm laser and 530/30 nm bandpass filter. For phycoerythrin, data were collected with the 488-nm laser and 585/42 nm bandpass filter. For RFP, data were collected with the 561-nm laser and 580/20 nm bandpass filter. For Alexa Fluor 647, data were collected with the 637-nm laser and 666/27 or 661/16 nm bandpass filter. After acquisition, flow cytometry data were analyzed with Flowjo software.

Small-sample cDNA amplification

Outer ECM-attached cells and inner cells (~50 each) were microdissected separately at day 6 of morphogenesis, amplified in quadruplicate by poly(A) PCR as previously described[16, 22], and hybridized to HumanRef-8 Expression BeadChips (Illumina). The ratio of inner/outer expression was calculated with amplification standard error calculated by error propagation.

Intraductal injections

Luciferase- and inducible shTNC-expressing MDA-MB-468 cells were treated with or without DOX for three days in culture and then suspended as single cells at a concentration of 20,000 cells/μl in MCF10A assay medium[12] containing 5 ng/ml EGF. Six- to ten-week-old female SCID-beige mice (Charles River) were split into treatment (with DOX) and control (without DOX) groups without formal randomization. Mice were anesthetized with isoflurane, and surgical scissors were used to cut a small crescent incision around the nipple to expose the inguinal gland. The tip of the nipple was snipped with surgical scissors, and a Hamilton syringe with a 30-gauge blunt-ended needle was used to deliver 2 μl of the cell suspension per gland (two glands per mouse). The crescent incisions were sealed with Gluture (Fisher), and mice were allowed to recover before returning to the animal facility. Treatment and control groups were fed standard rodent diet with or without DOX (Harlan). No statistical method was used to predetermine sample size, which was limited to the maximum number of surgeries that could be performed on one day. The investigators were not blinded to allocation during experiments and outcome assessment, and no animals were excluded from the study. All animal work was done in compliance with ethical regulations under IACUC approval #3945.

Bioluminescence imaging

Bioluminescent imaging was performed at 2, 7, 14, and 21 days post-injection on an IVIS Spectrum bioluminescence and fluorescence scanner (Caliper). During imaging, mice were anaesthetized with isoflurane and subsequently injected i.p. with 150 mg D-Luciferin/kg body weight. Bioluminescence imaging was initiated 5 minutes after injection with 2-minute exposure time until steady-state luminescence was reached. Bioluminescence photon fluxes were calculated using IVIS Imaging Spectrum Software.

Microarray accession numbers

Microarray data from Ref. [40] (Fig. 4a) are available through the NCBI Gene Expression Omnibus under accession number GSE5460. The microarray data generated in this work (Fig. 6a,b,e) are available through the NCBI Gene Expression Omnibus under accession number GSE41527.

Statistical analysis

Quantitative PCR data (Fig. 3a-d and 6c,d) were assessed by Student's *t* test, whose suitability was verified by the *F* test for homogeneity of variances after Bonferroni correction for multiple hypothesis testing. Enrichment of the TGFBR3–JUND clusters (Fig. 4a) was assessed by the hypergeometric test. Flow cytometry data (Fig. 5h,j, 6k, and 8e) was assessed by Welch's *t* test, with the exception of the shTNC apoptotic signatures (Fig. 8g), which were assessed by two-way ANOVA for an interaction between TNC knockdown and the frequencies of early-vs.-late apoptosis. Frequency of ductal colonization (Fig. 8f) was assessed by Fisher's exact test. Acinar areas (Supplementary Figure 3g) were compared by rank sum test. Cell numbers (Supplementary Figure 3h) and RNA FISH expression frequencies (Supplementary Figure 3j,l) were compared by Welch's *t* test. Comparison of

intraductal injections (Supplementary Figure 8d) was performed by Welch's *t* test after log transformation.

Replication of experiments

Immunoblot images (Fig. 2b,e,h, 5g, 6i,j, 8a,d and Supplementary Figure 3a,d, 5b,d,e, 6a,c,e,h, 7k, 8c) are representative of 2–3 independent experiments. RNA FISH images (Fig. 1c,d, 2d,f and Supplementary Figure 3i,k) are representative of 3–5 independent hybridizations. Immunofluorescence images (Fig. 4c,d,g,j,k, 5a-c,i,k, 6h,l, 7a-d,g and Supplementary Figure 2a, 3b,e, 4, 5a, 6b,d,f,i, 7c-iw, 8a,b) are representative of 2–3 independent in vitro experiments or at-least three separate fields per clinical specimen (since independent experiments on each clinical specimen could not be performed). Immunohistochemistry images (Fig. 4b, 8h-k and Supplementary Figure 8e) are representative of at-least three fields per specimen. Flow cytometry plots (Supplementary Figure 5c, 6g, 7l) are representative of four independent samples.

Supplementary Material

Refer to Web version on PubMed Central for supplementary material.

ACKNOWLEDGMENTS

REFERENCES

1. Altschuler SJ, Wu LF. Cellular heterogeneity: do differences make a difference? Cell. 2010; 141:559–563. [PubMed: 20478246]

2. Raj A, van Oudenaarden A. Nature, nurture, or chance: stochastic gene expression and its consequences. Cell. 2008; 135:216–226. [PubMed: 18957198]

3. Wernet MF, et al. Stochastic spineless expression creates the retinal mosaic for colour vision. Nature. 2006; 440:174–180. [PubMed: 16525464]

4. Laslo P, et al. Multilineage transcriptional priming and determination of alternate hematopoietic cell fates. Cell. 2006; 126:755–766. [PubMed: 16923394]

5. Raj A, Rifkin SA, Andersen E, van Oudenaarden A. Variability in gene expression underlies incomplete penetrance. Nature. 2010; 463:913–918. [PubMed: 20164922]

6. Shipitsin M, et al. Molecular definition of breast tumor heterogeneity. Cancer Cell. 2007; 11:259–273. [PubMed: 17349583]

7. Singh DK, et al. Patterns of basal signaling heterogeneity can distinguish cellular populations with different drug sensitivities. Mol Syst Biol. 2010; 6:369. [PubMed: 20461076]

8. Sharma SV, et al. A chromatin-mediated reversible drug-tolerant state in cancer cell subpopulations. Cell. 2010; 141:69–80. [PubMed: 20371346]

9. Elowitz MB, Levine AJ, Siggia ED, Swain PS. Stochastic gene expression in a single cell. Science. 2002; 297:1183–1186. [PubMed: 12183631]

10. Spencer SL, Gaudet S, Albeck JG, Burke JM, Sorger PK. Non-genetic origins of cell-to-cell variability in TRAIL-induced apoptosis. Nature. 2009; 459:428–432. [PubMed: 19363473]

11. Wang CC, Jamal L, Janes KA. Normal morphogenesis of epithelial tissues and progression of epithelial tumors. Wiley Interdiscip Rev Syst Biol Med. 2012; 4:51–78. [PubMed: 21898857]

12. Debnath J, Muthuswamy SK, Brugge JS. Morphogenesis and oncogenesis of MCF-10A mammary epithelial acini grown in three-dimensional basement membrane cultures. Methods. 2003; 30:256–268. [PubMed: 12798140]

13. Ewald AJ, Brenot A, Duong M, Chan BS, Werb Z. Collective epithelial migration and cell rearrangements drive mammary branching morphogenesis. Dev Cell. 2008; 14:570–581. [PubMed: 18410732]

14. Sato T, et al. Single Lgr5 stem cells build crypt-villus structures in vitro without a mesenchymal niche. Nature. 2009; 459:262–265. [PubMed: 19329995]

15. Debnath J, et al. The role of apoptosis in creating and maintaining luminal space within normal and oncogene-expressing mammary acini. Cell. 2002; 111:29–40. [PubMed: 12372298]

16. Janes KA, Wang CC, Holmberg KJ, Cabral K, Brugge JS. Identifying single-cell molecular programs by stochastic profiling. Nat Methods. 2010; 7:311–317. [PubMed: 20228812]

17. Shackleton M, et al. Generation of a functional mammary gland from a single stem cell. Nature. 2006; 439:84–88. [PubMed: 16397499]

18. Al-Hajj M, Wicha MS, Benito-Hernandez A, Morrison SJ, Clarke MF. Prospective identification of tumorigenic breast cancer cells. Proc Natl Acad Sci U S A. 2003; 100:3983–3988. [PubMed: 12629218]

19. Debnath J, Brugge JS. Modelling glandular epithelial cancers in three-dimensional cultures. Nat Rev Cancer. 2005; 5:675–688. [PubMed: 16148884]

20. Laakso M, et al. Basoluminal carcinoma: a new biologically and prognostically distinct entity between basal and luminal breast cancer. Clin Cancer Res. 2006; 12:4185–4191. [PubMed: 16857790]

21. van de Rijn M, et al. Expression of cytokeratins 17 and 5 identifies a group of breast carcinomas with poor clinical outcome. Am J Pathol. 2002; 161:1991–1996. [PubMed: 12466114]

22. Wang L, Janes KA. Stochastic profiling of transcriptional regulatory heterogeneities in tissues, tumors and cultured cells. Nat Protoc. 2013; 8:282–301. [PubMed: 23306461]

23. Wang XF, et al. Expression cloning and characterization of the TGF-beta type III receptor. Cell. 1991; 67:797–805. [PubMed: 1657407]

24. Nakashima M, Toyono T, Akamine A, Joyner A. Expression of growth/differentiation factor 11, a new member of the BMP/TGFbeta superfamily during mouse embryogenesis. Mech Dev. 1999; 80:185–189. [PubMed: 10072786]

25. Ahmed AA, et al. The extracellular matrix protein TGFBI induces microtubule stabilization and sensitizes ovarian cancers to paclitaxel. Cancer Cell. 2007; 12:514–527. [PubMed: 18068629]

26. Schmelzle T, et al. Functional role and oncogene-regulated expression of the BH3-only factor Bmf in mammary epithelial anoikis and morphogenesis. Proc Natl Acad Sci U S A. 2007; 104:3787–3792. [PubMed: 17360431]

27. Jensen RA, Page DL. Ductal carcinoma in situ of the breast: impact of pathology on therapeutic decisions. Am J Surg Pathol. 2003; 27:828–831. [PubMed: 12766588]

28. Tyson JJ, Chen KC, Novak B. Sniffers, buzzers, toggles and blinkers: dynamics of regulatory and signaling pathways in the cell. Curr Opin Cell Biol. 2003; 15:221–231. [PubMed: 12648679]

29. Berger I, Shaul Y. Structure and function of human jun-D. Oncogene. 1991; 6:561–566. [PubMed: 1903194]

30. Hempel N, et al. Expression of the type III TGF-beta receptor is negatively regulated by TGF-beta. Carcinogenesis. 2008; 29:905–912. [PubMed: 18299279]

31. Tsai TY, et al. Robust, tunable biological oscillations from interlinked positive and negative feedback loops. Science. 2008; 321:126–129. [PubMed: 18599789]

32. Nagai T, et al. A variant of yellow fluorescent protein with fast and efficient maturation for cell-biological applications. Nat Biotechnol. 2002; 20:87–90. [PubMed: 11753368]

33. Li X, et al. Generation of destabilized green fluorescent protein as a transcription reporter. J Biol Chem. 1998; 273:34970–34975. [PubMed: 9857028]

34. Dantuma NP, Lindsten K, Glas R, Jellne M, Masucci MG. Short-lived green fluorescent proteins for quantifying ubiquitin/proteasome-dependent proteolysis in living cells. Nat Biotechnol. 2000; 18:538–543. [PubMed: 10802622]

35. Kearns JD, Basak S, Werner SL, Huang CS, Hoffmann A. IkappaBepsilon provides negative feedback to control NF-kappaB oscillations, signaling dynamics, and inflammatory gene expression. J Cell Biol. 2006; 173:659–664. [PubMed: 16735576]

36. Schneyer AL, et al. Differential antagonism of activin, myostatin and growth and differentiation factor 11 by wild-type and mutant follistatin. Endocrinology. 2008; 149:4589–4595. [PubMed: 18535106]

37. Taipale J, Saharinen J, Hedman K, Keski-Oja J. Latent transforming growth factor-beta 1 and its binding protein are components of extracellular matrix microfibrils. J Histochem Cytochem. 1996; 44:875–889. [PubMed: 8756760]

38. Rakha EA, Reis-Filho JS, Ellis IO. Basal-like breast cancer: a critical review. J Clin Oncol. 2008; 26:2568–2581. [PubMed: 18487574]

39. Bryan BB, Schnitt SJ, Collins LC. Ductal carcinoma in situ with basal-like phenotype: a possible precursor to invasive basal-like breast cancer. Mod Pathol. 2006; 19:617–621. [PubMed: 16528377]

40. Lu X, Wang ZC, Iglehart JD, Zhang X, Richardson AL. Predicting features of breast cancer with gene expression patterns. Breast Cancer Res Treat. 2008; 108:191–201. [PubMed: 18297396]

41. Dong M, et al. The type III TGF-beta receptor suppresses breast cancer progression. J Clin Invest. 2007; 117:206–217. [PubMed: 17160136]

42. Wang L, Brugge JS, Janes KA. Intersection of FOXO- and RUNX1-mediated gene expression programs in single breast epithelial cells during morphogenesis and tumor progression. Proc Natl Acad Sci U S A. 2011; 108:E803–E812. [PubMed: 21873240]

43. Azzopardi JG, Ahmed A, Millis RR. Problems in breast pathology. Major Probl Pathol. 1979; 11:193–203.

44. Reginato MJ, et al. Integrins and EGFR coordinately regulate the pro-apoptotic protein Bim to prevent anoikis. Nat Cell Biol. 2003; 5:733–740. [PubMed: 12844146]

45. Muthuswamy SK, Li D, Lelievre S, Bissell MJ, Brugge JS. ErbB2, but not ErbB1, reinitiates proliferation and induces luminal repopulation in epithelial acini. Nat Cell Biol. 2001; 3:785–792. [PubMed: 11533657]

46. Bhowmick NA, Neilson EG, Moses HL. Stromal fibroblasts in cancer initiation and progression. Nature. 2004; 432:332–337. [PubMed: 15549095]

47. Candi E, Schmidt R, Melino G. The cornified envelope: a model of cell death in the skin. Nat Rev Mol Cell Biol. 2005; 6:328–340. [PubMed: 15803139]

48. Mailleux AA, et al. BIM regulates apoptosis during mammary ductal morphogenesis, and its absence reveals alternative cell death mechanisms. Dev Cell. 2007; 12:221–234. [PubMed: 17276340]

49. Malik RK, Parsons JT. Integrin-dependent activation of the p70 ribosomal S6 kinase signaling pathway. J Biol Chem. 1996; 271:29785–29791. [PubMed: 8939916]

50. Gan B, Yoo Y, Guan JL. Association of focal adhesion kinase with tuberous sclerosis complex 2 in the regulation of s6 kinase activation and cell growth. J Biol Chem. 2006; 281:37321–37329. [PubMed: 17043358]

51. Schalm SS, Blenis J. Identification of a conserved motif required for mTOR signaling. Curr Biol. 2002; 12:632–639. [PubMed: 11967149]

52. Uhlen M, et al. A human protein atlas for normal and cancer tissues based on antibody proteomics. Mol Cell Proteomics. 2005; 4:1920–1932. [PubMed: 16127175]

53. Uhlen M, et al. Towards a knowledge-based Human Protein Atlas. Nat Biotechnol. 2010; 28:1248–1250. [PubMed: 21139605]

54. Humphries JD, Byron A, Humphries MJ. Integrin ligands at a glance. J Cell Sci. 2006; 119:3901–3903. [PubMed: 16988024]

55. Jones PL, Jones FS. Tenascin-C in development and disease: gene regulation and cell function. Matrix Biol. 2000; 19:581–596. [PubMed: 11102748]

56. Oskarsson T, et al. Breast cancer cells produce tenascin C as a metastatic niche component to colonize the lungs. Nat Med. 2011; 17:867–874. [PubMed: 21706029]

57. Schalkwijk J, et al. Tenascin expression in human dermis is related to epidermal proliferation. Am J Pathol. 1991; 139:1143–1150. [PubMed: 1719820]

58. Thorne BC, Bailey AM, Peirce SM. Combining experiments with multi-cell agent-based modeling to study biological tissue patterning. Brief Bioinform. 2007; 8:245–257. [PubMed: 17584763]

59. Miller FR, Santner SJ, Tait L, Dawson PJ. MCF10DCIS.com xenograft model of human comedo ductal carcinoma in situ. J Natl Cancer Inst. 2000; 92:1185–1186. [PubMed: 10904098]

60. Behbod F, et al. An intraductal human-in-mouse transplantation model mimics the subtypes of ductal carcinoma in situ. Breast Cancer Res. 2009; 11:R66. [PubMed: 19735549]

61. Shi M, et al. Latent TGF-beta structure and activation. Nature. 2011; 474:343–349. [PubMed: 21677751]

62. Paszek MJ, et al. Tensional homeostasis and the malignant phenotype. Cancer Cell. 2005; 8:241–254. [PubMed: 16169468]

63. Ruvinsky I, et al. Ribosomal protein S6 phosphorylation is a determinant of cell size and glucose homeostasis. Genes Dev. 2005; 19:2199–2211. [PubMed: 16166381]

64. Tyner AL, Fuchs E. Evidence for posttranscriptional regulation of the keratins expressed during hyperproliferation and malignant transformation in human epidermis. J Cell Biol. 1986; 103:1945–1955. [PubMed: 2430980]

65. Ishihara A, Yoshida T, Tamaki H, Sakakura T. Tenascin expression in cancer cells and stroma of human breast cancer and its prognostic significance. Clin Cancer Res. 1995; 1:1035–1041. [PubMed: 9816077]

66. Gupta PB, et al. Stochastic state transitions give rise to phenotypic equilibrium in populations of cancer cells. Cell. 2011; 146:633–644. [PubMed: 21854987]

67. Cheung KJ, Gabrielson E, Werb Z, Ewald AJ. Collective invasion in breast cancer requires a conserved Basal epithelial program. Cell. 2013; 155:1639–1651. [PubMed: 24332913]

68. Moffat J, et al. A lentiviral RNAi library for human and mouse genes applied to an arrayed viral high-content screen. Cell. 2006; 124:1283–1298. [PubMed: 16564017]

69. Shin KJ, et al. A single lentiviral vector platform for microRNA-based conditional RNA interference and coordinated transgene expression. Proc Natl Acad Sci U S A. 2006; 103:13759–13764. [PubMed: 16945906]

70. Miller-Jensen K, Janes KA, Brugge JS, Lauffenburger DA. Common effector processing mediates cell-specific responses to stimuli. Nature. 2007; 448:604–608. [PubMed: 17637676]

Author Manuscript

Author Manuscript

Author Manuscript

Author Manuscript
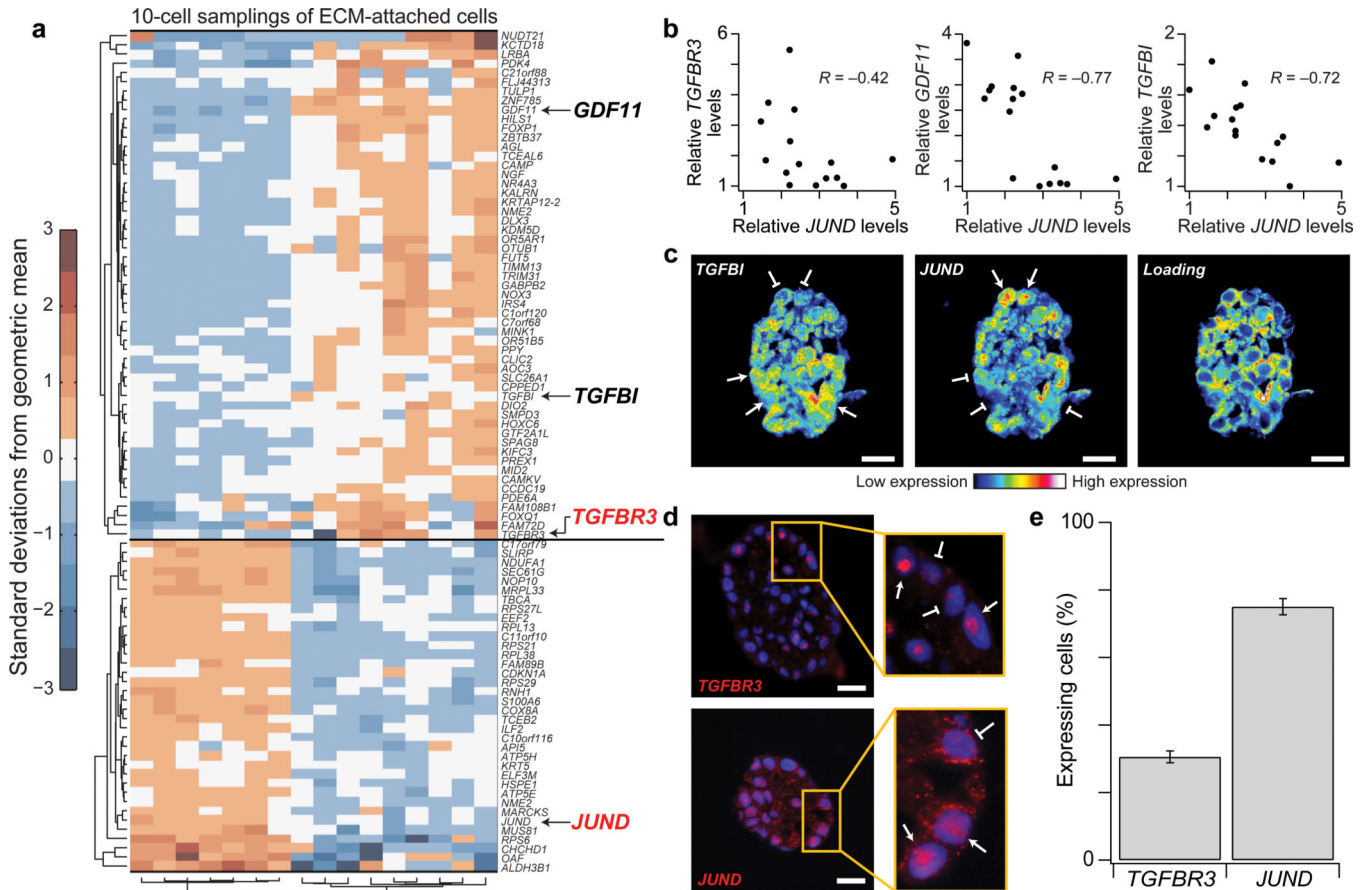
Figure 1.
TGFBR3 and *JUND* lie within anticorrelated single-cell expression programs among ECM-attached basal-like cells in organotypic 3D culture. (**a**) Hierarchical clustering of sampling fluctuations for the *TGFBR3* and *JUND* anticorrelated expression programs identified by stochastic sampling of ECM-attached cells at day 10 of acinar morphogenesis[16]. 10-cell sampling data were scaled to log unit variance and clustered by Euclidean distance with Ward's linkage. (**b**) Stochastic-profiling anticorrelations between *JUND* and *TGFBR3, GDF11*, and *TGFBI*. The Pearson correlation (*R*) of n=16 independent 10-cell samples is indicated. (**c**) Three-color RNA fluorescence in situ hybridization (RNA FISH) images showing anticorrelated expression between *JUND* and *TGFBI*. Images are pseudocolored to highlight quantitative differences in fluorescence intensity, and single cells showing strong anticorrelation are highlighted with arrows (high expression) or flat markers (low expression). A combination of three housekeeping genes (*GAPDH, HINT1, PRDX6*) was used as control for total cellular mRNA levels[42]. (**d**) *TGFBR3* and *JUND* show inverse frequencies of heterogeneous expression by RNA FISH. Active *JUND* and *TGFBR3* transcription appears as nascent foci in the nucleus (arrows). Cells with weak expression are indicated with flat markers. Cells were counterstained with DAPI (blue) to label nuclei. (**e**) Quantification of *TGFBR3* and *JUND* expression frequencies within matrix-attached cells. For (**c**) and (**d**), scale bar is 20 μm. For (**e**), data are shown as the mean ± s.e.m. of n=4 independent hybridizations. For source data, see Supplementary Table 3.
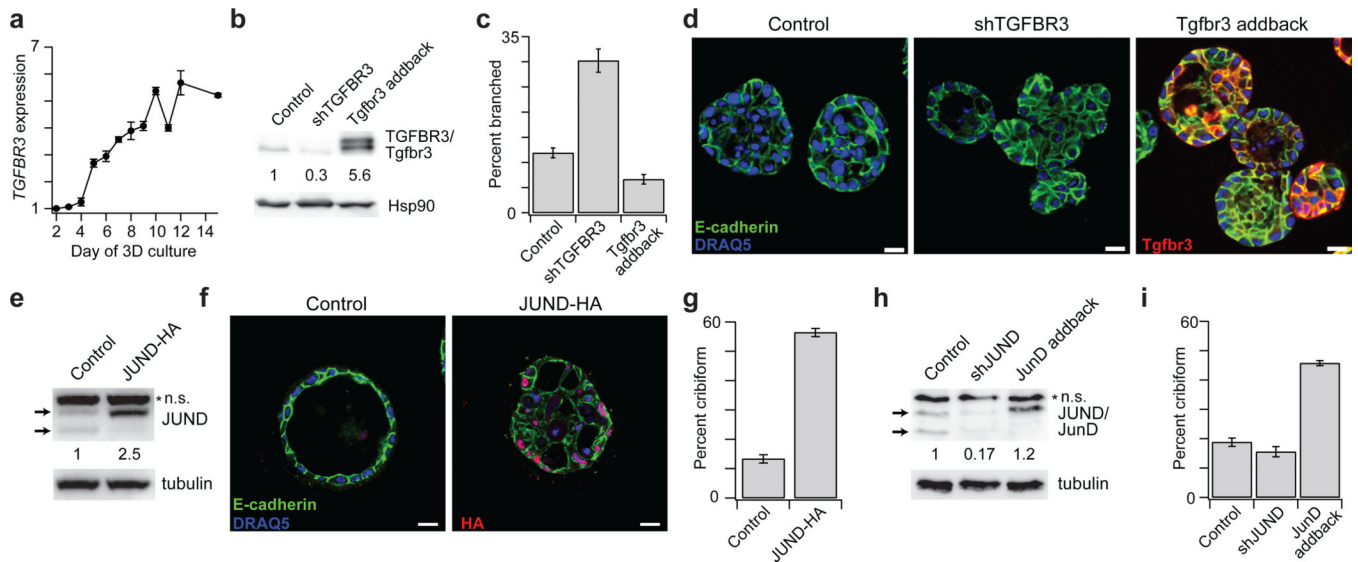
Figure 2.
TGFBR3 and JUND are functionally important for 3D morphogenesis. (**a**) Time-dependent expression of *TGFBR3* during 3D morphogenesis[26]. (**b**) Knockdown of TGFBR3 and inducible addback of murine RNAi-resistant Tgfbr3. TGFBR3/Tgfbr3 levels for cells cultured in the absence (Lane 1 and 2) or presence (Lane 3) of 1 μg/ml DOX for 24 hours were analyzed by immunoblotting. Hsp90 was used as a loading control. Densitometry of TGFBR3/Tgfbr3 abundance is shown normalized to the shGFP control. (**c** and **d**) Blocking TGFBR3 induction specifically elicits a ductal-branching phenotype. The MCF10A-5E lines described in (**b**) were placed in morphogenesis in the absence (control and shTGFBR3) or presence (Tgfbr3 addback) of 1 μg/ml DOX from day 4–10. Acini were fixed at day 10 of 3D culture, stained for E-cadherin (green) and HA-tagged Tgfbr3 (red), and analyzed by confocal immunofluorescence. Cells were counterstained with DRAQ5 (blue) to label nuclei. (**e**) Constitutive expression of HA-tagged JUND analyzed by immunoblotting. Densitometry of JUND abundance is shown normalized to pBabe vector control. (**f** and **g**) Constitutive JUND expression causes stable cribiform-like acinar structures. Acini from the MCF10A-5E lines described in (**e**) were placed in morphogenesis, fixed at day 28, stained for E-cadherin (green) and HA-tagged JUND (red), and analyzed by confocal immunofluorescence. Cells were counterstained with DRAQ5 (blue) to label nuclei. (**h**) Homogenization of JUND expression by knockdown of JUND and addback with murine RNAi-resistant JunD to near-endogenous expression levels. JUND/JunD levels were determined by immunoblotting. Densitometry of JUND/JunD abundance is shown normalized to the shGFP control. (**i**) Quantification of the cribiform-like phenotype at day 28 of 3D culture for the cells in (**h**). For (**a**), (**c**), (**g**), and (**i**), data are shown as the mean ± s.e.m. of n=3 (**a**) or n=4 (**c, g, i**) independent experiments. For (**d**) and (**f**), scale bar is 20 μm. For (**e**) and (**h**), tubulin was used as a loading control and n.s. denotes a non-specific band. For source data, see Supplementary Table 3.
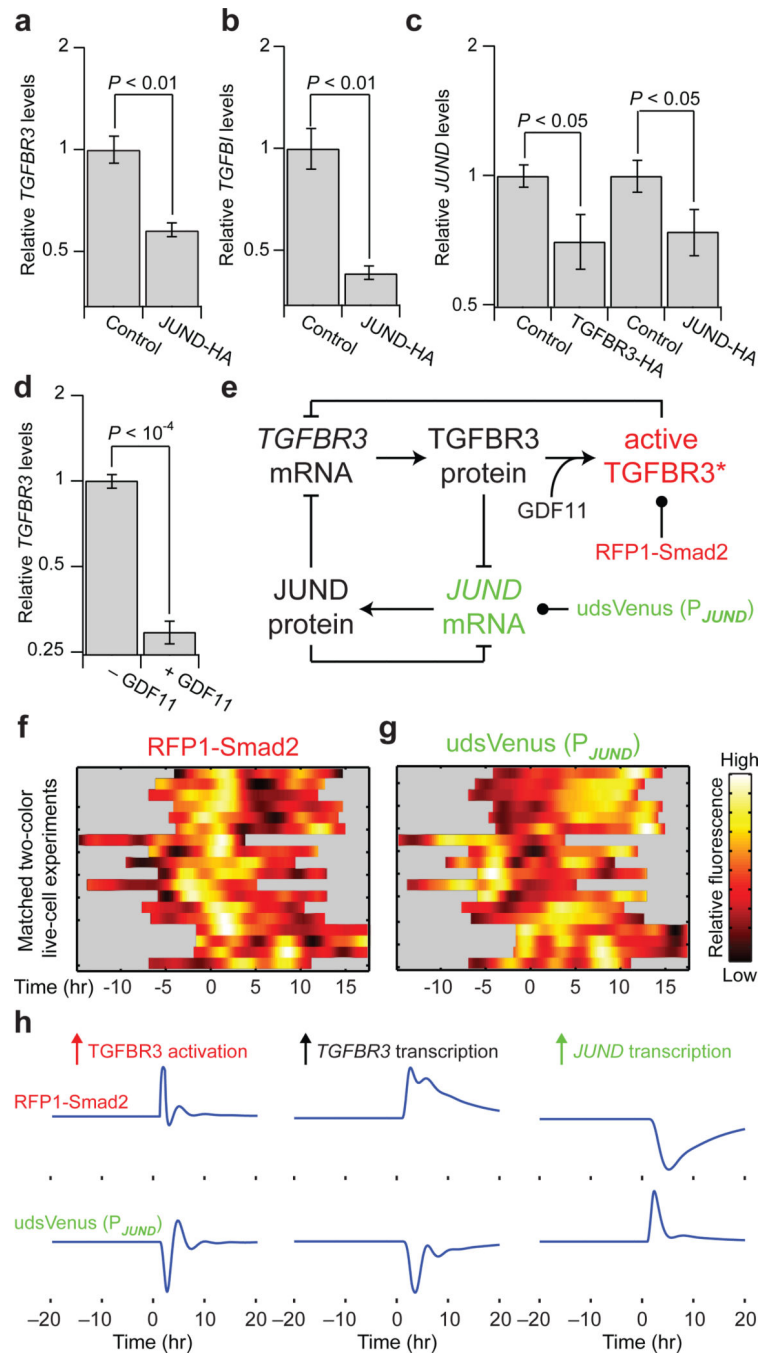
Figure 3.
JUND transcription and TGFβ-family signaling activity are functionally and dynamically coupled. (**a** and **b**) *TGFBR3* and *TGFBI* are repressed by constitutive JUND expression. (**c**) Endogenous *JUND* is repressed by constitutive expression of TGFBR3 or JUND. (**d**) *TGFBR3* is negatively regulated by TGFβ-family signaling. (**e**) Schematic of positive and negative feedback loops connecting *TGFBR3* and *JUND*. The arrows and flat markers indicate the positive and negative relationships from (**a–d**). Black circles indicate the two fluorescent reporters (RFP1-Smad2 and udsVenus (P$_{JUND}$)) used to monitor the single-cell

dynamics of TGFβ-family activity and *JUND* promoter activity. (**f** and **g**) Multiple alignment of dynamic single-cell fluorescence trajectories. Two-color live-cell confocal imaging was used to quantify the level of nuclear RFP1-Smad2 (left) and total udsVenus (P*JUND*) expression (right) of ECM-attached cells at day 10 of morphogenesis. Gray indicates no data. (**h**) Damped oscillations in an ordinary differential equations model of the TGFBR3–JUND expression circuit induced by TGFBR3 activation (left; RFP1-Smad2 range: [11.5–15.7], udsVenus (P$_{JUND}$) range: [13.0–20.6]), *TGFBR3* upregulation (middle; RFP1-Smad2 range: [12.1–23.2], udsVenus (P$_{JUND}$) range: [0.745–18.4]), or *JUND* upregulation (right; RFP1-Smad2 range: [3.80–12.1], udsVenus (P$_{JUND}$) range: [18.4–65.2]). In the model, the basal transcription rate was 4 hr^{-1}, the basal translation rate was 100 $mRNA^{-1}$ hr^{-1}, the mRNA degradation rate was 0.23 hr^{-1}, the degradation of TGFBR3 protein was 3 hr^{-1}, the degradation of JUND protein was 0.37 hr^{-1}, the degradation of udsVenus was 2.8 hr^{-1}, and the activation rate of TGFBR3 was 1 hr^{-1} (Supplementary Note 1). For (**a–c**), MCF10A-5E cells stably expressing JUND-HA, TGFBR3–HA, or vector control were placed in 3D culture and analyzed at day 10 of morphogenesis by quantitative PCR for the indicated genes. Endogenous *JUND* was analyzed with primers specific for the 3' UTR of *JUND*. For (**d**), MCF10A-5E cells were stimulated with 250 ng/ml GDF11 for 4 hr and analyzed for *TGFBR3* expression. Data are shown as the mean ± s.e.m. of n=4 independent samples, and *P* values were calculated by Student's one-sided *t* test. For simulation code and source data, see Supplementary Data File 1 and Supplementary Table 3.
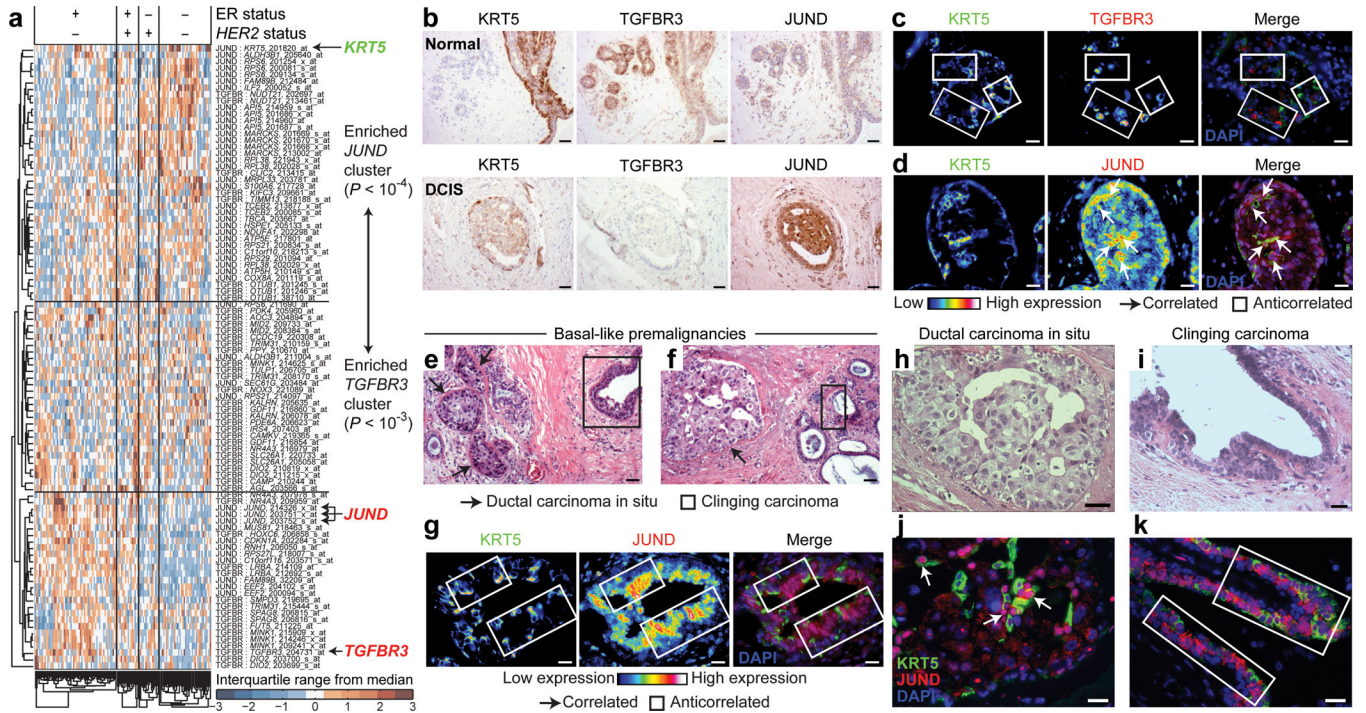
Figure 4.

TGFBR3 and JUND expression reciprocally map to KRT5 in specific regions of heterogeneous basal-like premalignancies. (**a**) Enriched clusters of *JUND*- and *TGFBR3*-associated transcripts contain neither *JUND* nor *TGFBR3* among various subtypes of breast carcinoma. Transcripts from Fig. 1a were extracted from Ref. [40], standardized nonparametrically, and arranged by unsupervised hierarchical clustering based on Euclidean distance with Ward's linkage. Enrichment *P* values for *TGFBR3*- and *JUND*-cluster genes in the two upper branches of the dendrogram were calculated by hypergeometric test. Estrogen receptor (ER) and *HER2* status is indicated according to Ref. [40]. (**b**) KRT5, TGFBR3, and JUND immunohistochemistry in normal breast tissue and basal-like DCIS. (**c**) Expression of TGFBR3 and KRT5 proteins is mutually exclusive in ER-negative premalignant lesions. (**d**) Expression of JUND and KRT5 proteins is correlated in ER-negative ductal carcinoma in situ (DCIS). (**e–f**) Paraffin sections from two cases of basal-like DCIS (arrows) were stained with hematoxylin and eosin and visualized by brightfield microscopy. Regions of clinging carcinoma are highlighted with rectangles. (**g**) Expression of JUND and KRT5 is anticorrelated in peripheral regions of clinging carcinoma. (**h–k**) Local inversion of the JUND–KRT5 correlation in the same patient. Note in (**j**) that KRT5 is coexpressed with JUND in the DCIS, whereas in (**k**) KRT5 is anticorrelated with JUND in peripheral regions of clinging carcinoma. For (**c**), (**d**), (**g**), (**j**), and (**k**), paraffin sections from basal-like premalignant lesions were stained for KRT5 (green) and TGFBR3 (red; **c**) or JUND (red; **d**, **g**, **j**, **k**) and imaged by widefield immunofluorescence. Nuclei were counterstained with DAPI (blue). Single-color fluorescence images are pseudocolored in the first two subpanels of (**c**), (**d**), and (**g**) to highlight quantitative differences in immunoreactivity. Correlated and anticorrelated regions of expression are indicated with arrows and rectangles respectively.

Scale bars are 20 μm (**c–d**, **g–h**, **j–k**), 40 μm (**i**), and 80 μm (**b**, **e**, **f**). For source data, see Supplementary Table 3.
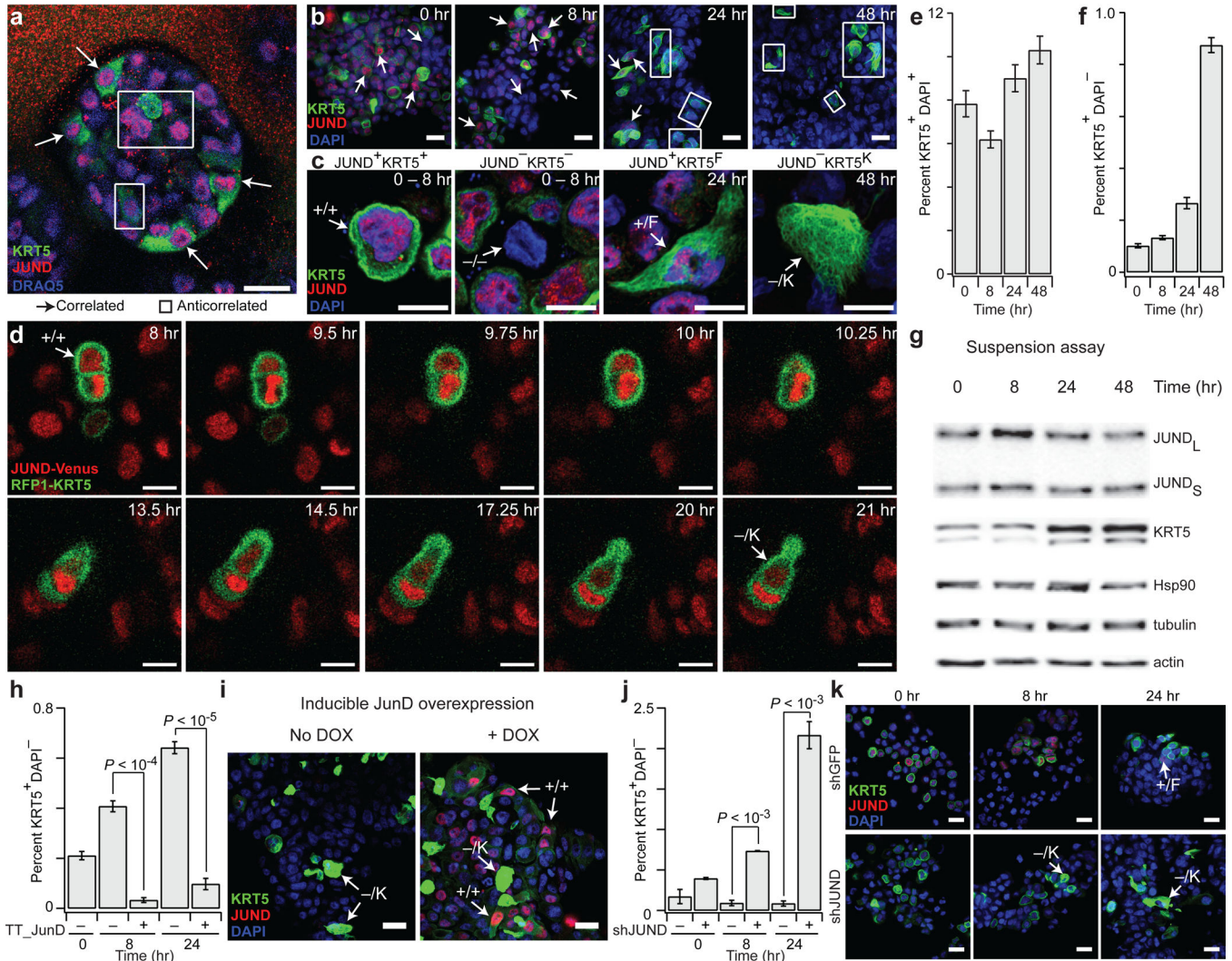
Figure 5.
JUND and KRT5 become anticorrelated via keratinization induced by prolonged ECM detachment. (**a**) The JUND–KRT5 correlation state depends on attachment to basement membrane during epithelial acinar morphogenesis. MCF10A-5E acini were fixed at day 10 of morphogenesis, stained for KRT5 (green) and JUND (red), and analyzed by confocal immunofluorescence. Cells were counterstained with DRAQ5 (blue) to label nuclei. (**b** and **c**) Loss of ECM-attachment induces keratinization and JUND–KRT5 anticorrelation. MCF10A-5E cells were placed in polyHEMA-coated plates with assay medium containing 5 ng/ml EGF. (**d**) Epithelial keratinization occurs rapidly during cell detachment. MCF10A-5E cells stably expressing JUND-Venus (false-color red) and RFP1-KRT5 (false-color green) were placed in suspension with assay medium containing 5 ng/ml EGF. Two-color live-cell confocal images were collected after the indicated times in suspension. (**e** and **f**) Flow cytometry quantification of high KRT5 (KRT+–DAPI−; **e**) and keratinized (KRT5+–DAPI−; **f**) cells as a function of time in suspension. (**g**) KRT5 protein expression is upregulated during detachment. MCF10A-5E cells were placed in suspension for the indicated times. (**h–k**) JUND delays the terminal steps of keratinization. MCF10A-5E cells

were transduced with doxycycline (DOX)-inducible JUND-HA (**h** and **i**) or shJUND or shGFP control (**j** and **k**) and placed in suspension culture for the indicated times. For (**a**) and (**b**), correlated and anticorrelated regions of expression are indicated with arrows and rectangles respectively. For (**b**), (**c**), (**i**), and (**k**), cells were fixed at the indicated times, stained for KRT5 (green) and JUND (red), and analyzed by confocal immunofluorescence. Cells were counterstained with DAPI (blue) to label nuclei. For (**g**), JUND and KRT5 levels were analyzed by immunoblotting with Hsp90 tubulin, and actin used as loading controls. JUND appears as both short ($JUND_S$) and long ($JUND_L$) forms. For (**e**), (**f**), (**h**), and (**j**), flow cytometry data are shown as the mean ± s.e.m. of n=4 independent biological samples, and *P* values were calculated by Welch's two-sided *t* test.. For (**a**), (**b**), (**i**), and (**k**), scale bar is 20 μm. For (**c**), scale bar is 10 μm. For (**c**), (**i**), and (**k**), single cells representing intermediate stages of keratinization are highlighted with arrows. For source data, see Supplementary Table 3.
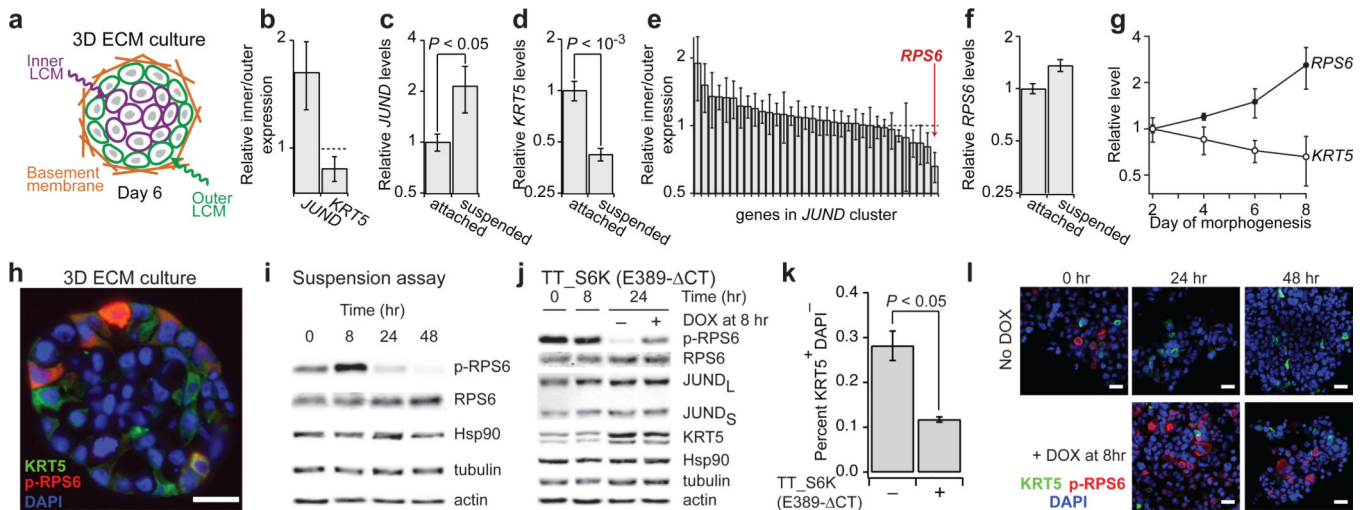
Figure 6.
Basal-cell keratinization is triggered by the loss of RPS6 phosphorylation. (**a**) Laser-capture microdissection (LCM) scheme for profiling inner and outer cells during morphogenesis. (**b–d**) *JUND* expression is increased and *KRT5* expression is decreased in inner acinar cells and during ECM detachment. (**e**) An expression-profiling screen identifies *RPS6* as disproportionately under-expressed in inner acinar cells. (**f** and **g**) *RPS6* expression is not decreased during ECM detachment but increases during morphogenesis. (**h**) RPS6 phosphorylation is heterogeneous in outer ECM-attached cells and absent in inner cells during morphogenesis. Day 10 frozen sections of MCF10A-5E acini were stained for KRT5 (green) and phospho-RPS6 (p-RPS6, red) and imaged by widefield immunofluorescence. Cells were counterstained with DAPI (blue) to label nuclei. (**i**) p-RPS6 is lost during detachment. MCF10A-5E cells were placed in suspension for the indicated times. Loading controls are reprinted from Fig. 5g. (**j–l**) Maintaining RPS6 phosphorylation inhibits detachment-induced KRT5 upregulation. MCF10A-5E cells were transduced with DOX-inducible S6K (E389- CT), placed in suspension culture, and then induced with 1 μg/ml DOX after 8 hr. For (**b**) and (**e**), microarray data are shown as the mean ± s.e.m. of four separate 10-cell amplifications. For (**c**), (**d**), and (**f**), MCF10A-5E cells were placed in suspension or in culture dishes for 48 hr and analyzed for the indicated genes by quantitative PCR. Data are shown as the mean ± s.e.m. of n=4 independent biological samples, and *P* values were calculated by Student's two-sided *t* test. For (**g**), MCF10A-5E cells were placed in 3D culture and analyzed for the indicated genes by quantitative PCR. Data are shown as the mean ± s.e.m. of n=3 independent biological samples. For (**k**), flow cytometry data are shown as the mean ± s.e.m. of n=4 independent biological samples, and *P* values were calculated by Welch's two-sided *t* test. For (**i**) and (**j**), cells were analyzed by immunoblotting for the indicated proteins with Hsp90, tubulin, and actin used as loading controls. For (**h**) and (**l**), cells were fixed at the indicated times and stained for KRT5 (green), p-RPS6 (red), and analyzed by widefield or confocal immunofluorescence. Cells were counterstained with DAPI (blue) to label nuclei. For (**h**) and (**l**), scale bar is 20 μm. For source data, see Supplementary Table 3.
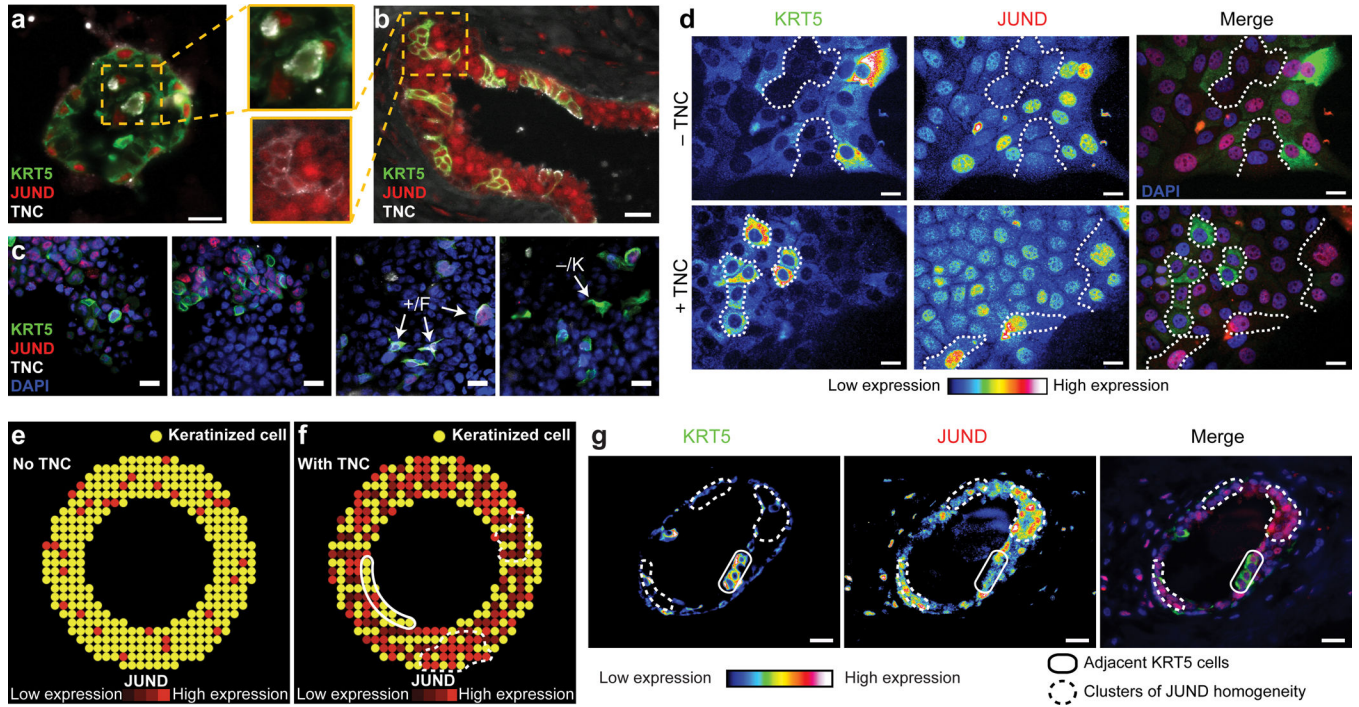
Figure 7.
JUND–KRT5 mosaicism in ECM-poor microenvironments is stabilized by TNC. (**a** and **b**) The JUND–KRT5 anticorrelation state reflects a microenvironment that lacks basement membrane but contains TNC. Day 10 frozen sections of MCF10-5E acini (**a**) and paraffin sections from premalignant basal-like neoplasms (**b**) were stained for KRT5 (green), JUND (red), and TNC (white) and imaged by widefield immunofluorescence. (**c**) TNC protein expression is upregulated during detachment. MCF10A-5E cells were placed in suspension for the indicated times. Cells were fixed and stained for KRT5 (green), JUND (red), and TNC (white) and analyzed by confocal immunofluorescence. Cells were counterstained with DAPI (blue) to label nuclei. (**d**) The JUND–KRT5 correlation is reversed *in vitro* by exogenous TNC. MCF10A-5E cells were grown on coverslips in assay medium[12] + 5 ng/ml EGF in the presence or absence of 5 μg/ml TNC for 8 days. The cells were stained with antibodies against KRT5 (green) and JUND (red) and imaged by widefield immunofluorescence. Nuclei were counterstained with DAPI (blue). In the first two panels, single-color fluorescence images are pseudocolored to highlight quantitative differences in immunoreactivity. Dashed lines separate regions that stain strongly or weakly for KRT5 expression. (**e** and **f**) An agent-based model requires a TNC-like molecule to stabilize JUND–KRT5 expression patterns. Solid lines highlight strings of keratinized cells adjacent to the lumen (yellow). Dashed lines highlight clusters of locally homogeneous JUND expression (red). (**g**) Paraffin sections from early basal-like carcinomas were stained for KRT5 (green) and JUND (red) and imaged by widefield immunofluorescence. Nuclei were counterstained with DAPI (blue). In first two panels, single-color fluorescence images are pseudocolored to highlight quantitative differences in immunoreactivity. Strings of keratinized cells (solid) and clusters of local JUND homogeneity (dashed) are highlighted. For (**a–d**) and (**g**), scale bar is 20 μm. For simulation code, see Supplementary Data File 2.
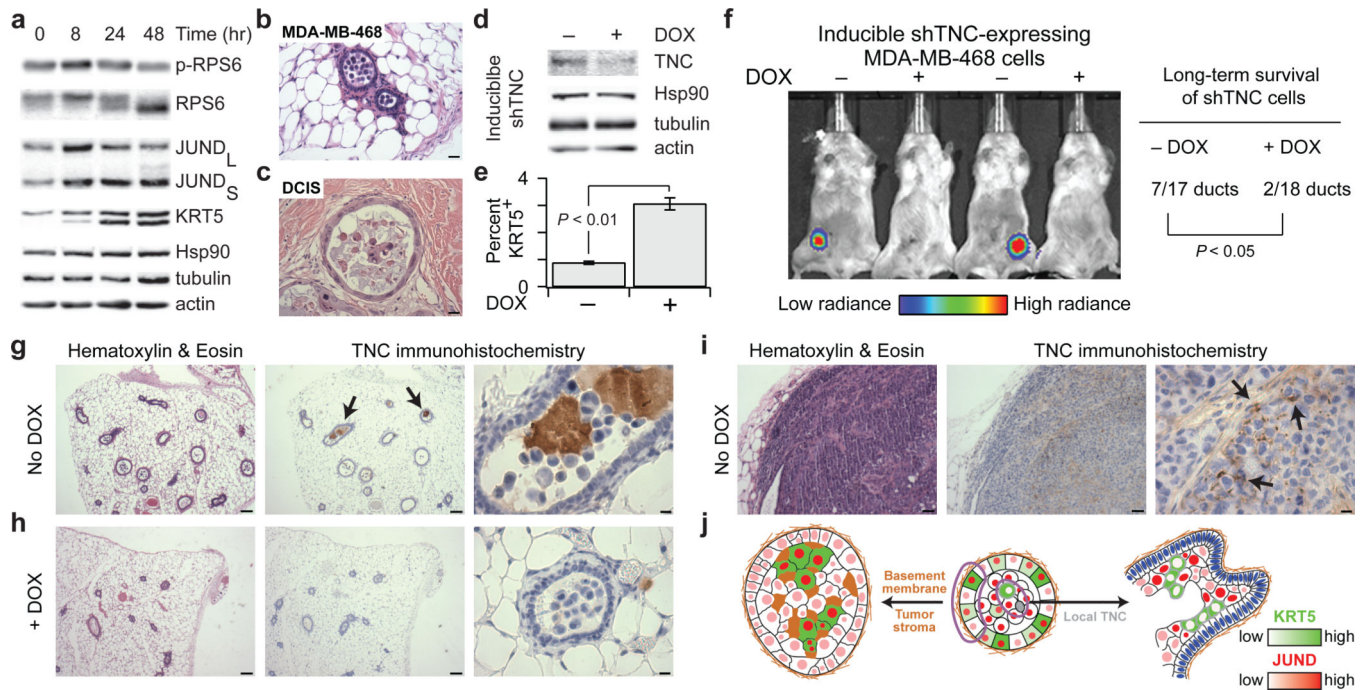
Figure 8.
Juxtacrine TNC promotes intraductal colonization of basal-like human breast cancer cells *in vivo*. (**a**) Changes in RPS6 phosphorylation, JUND, and KRT5 in MDA-MB-468 cells placed in suspension for the indicated times. JUND appears as both short ($JUND_S$) and long ($JUND_L$) forms. (**b** and **c**) An intraductal xenograft model of human DCIS. Hematoxylin and eosin histology of a SCID-beige mammary duct injected with MDA-MB-468 cells (**b**) compared to a clinical specimen of basal-like DCIS (**c**). (**d**) Validation of shTNC inducible knockdown cells. Luciferase-expressing MDA-MB-468 cells were infected with doxycycline (DOX)-inducible shTNC, stably selected, and treated with or without 1 μg/ml DOX for three days in culture before detachment for 24 hours. (**e**) Frequency of $KRT5^+$ cells after TNC knockdown was assessed by flow cytometry. MDA-MB-468 cells were treated with or without 1 μg/ml DOX for three days. (**f**) TNC-dependent intraductal colonization of MDA-MB-468 cells in SCID-beige mice at 21 days post-injection. Frequency of stable intraductal colonization was compared by Fisher's exact test. (**g–i**) Paraffin sections from MDA-MB-468 intraductal xenografts were stained with hematoxylin and eosin (left) or TNC by immunohistochemistry (middle and right). The strong staining for TNC protein is highlighted with arrows. (**j**) Model for the relationship between 3D-tumor microenvironments and JUND-KRT5 coregulation. Outer ECM-attached cells in organotypic 3D culture mimic the stroma-rich microenvironment of the primary tumor (left). Inner ECM-deprived cells signal via juxtacrine TNC to invert the coregulation of JUND and KRT5 (right). For (**a**) and (**d**), cells were analyzed by immunoblotting for the indicated proteins with Hsp90, tubulin, and actin used as loading controls. For (**e**), flow cytometry data are shown as the mean ± s.e.m. of n=4 independent biological samples, and *P* values were calculated by Welch's two-sided *t* test. Scale bars are 20 μm (**g–i** right), 40 μm (**b–c**),

80 µm (**i** left and middle), and 200 µm (**g** and **h** left and middle). For source data, see Supplementary Table 3.